國立陽明交通大學

機械工程學系

碩士論文

Department of Mechanical Engineering

National Yang Ming Chiao Tung University

Master Thesis

基於積分同步學習之多軸無人機參數估測與控制

Parameter Estimation and Control of Multirotors Using Integral Concurrent Learning

研究生: 楊承澄 (Cheng-Cheng Yang)

指導教授: 程登湖 博士 (Teng-Hu Cheng)

中華民國一百一十年八月

August, 2021

基於積分同步學習之多軸無人機參數估測與控制

Parameter Estimation and Control of Multirotors Using Integral Concurrent Learning

研究生： 楊承澄　　Student： Cheng-Cheng Yang

指導教授： 程登湖 博士　　Advisor： Dr. Teng-Hu Cheng

國立陽明交通大學

機械工程學系

碩士論文

A Thesis
Submitted to Department of Mechanical Engineering
College of Engineering
National Yang Ming Chiao Tung University
in partial Fulfillment of the Requirements
for the Degree of
Master of Department of Mechanical Engineering
in
College of Engineering

August, 2021

Taiwan, Republic of China

中華民國一百一十年八月

Acknowledegment

I would like to thank the following people, without whom I would not have been able to complete this research, and without whom I would not have made it through my master's degree!

1. The NCRL Lab. at National Yang Ming Chiao Tung University, especially to my advisor Dr. Teng-Hu Cheng, whose insight and knowledge into the subject matter steered me through this research.

2. My classmates and friends, who have supported me and given me useful advice, and had to put up with my stresses for the past two years of study!

3. And my biggest thanks to my family for all the support you have shown me in two years of learning.

基於積分同步學習之多軸無人機參數估測與控制

學生：楊承澄　　指導教授：程登湖 博士

國立陽明交通大學工學院機械工程學系碩士班

摘要

在本篇論文中，基於積分同步學習 (ICL) 之多軸無人機參數估測與控制演算法被完整開發，此控制演算法將被用來同時控制無人機與估測未知的無人機質量與轉動慣量。據我們所知，這是首個將同步學習應用於估測無人機之質量與轉動慣量上的研究，此控制演算法搭配幾何追蹤控制提供無人機迴授控制。在此研究中，由於無人機的動態是在全域的空間上定義，因此開發出來的 ICL 控制器可以確保全域的狀態誤差收斂與參數估測誤差收斂。此外，此控制架構可以被應用在任何未知質量與轉動慣量的無人機上。經由穩定性證明，狀態誤差與參數估測誤差會以漸近的形式收斂。ICL 控制器的性能與效率將會經由模擬與實驗結果展現。

關鍵字：多軸無人機、無人機控制、幾何追蹤控制、系統參數估測、自適應控制、積分同步學習

Parameter Estimation and Control of Multirotors Using Integral Concurrent Learning

Student : Cheng-Cheng Yang Advisor : Dr. Teng-Hu Cheng

Department of Mechanical Engineering of
National Yang Ming Chiao Tung University

ABSTRACT

A controller based on integral concurrent learning (ICL) has been developed for controlling a multirotor unmanned aerial vehicle with unknown mass and moment of inertia. To the best of our knowledge, this is the first study to use concurrent learning methods to estimate the mass and moment of inertia of a multirotor, which are incorporated in the geometric tracking controller to provide feedback. Since the dynamics of a multirotor is globally defined, the developed ICL controller ensures almost global tracking and parameter estimation. The developed control architecture can be generalized to control any multirotor of unknown mass and moment of inertia with guaranteed system stability. A stability analysis was conducted to ensure that both the tracking errors and the estimate errors of the parameters were asymptotic. The performance and efficacy of the ICL controller have been verified in simulations and experiments.

Keywords: multirotor unmanned aerial vehicle, control of the multirotor, geometric tracking controller, parameters estimation, adaptive control, integral concurrent learning

Table of Contents

List of Figures

List of Tables

Chapter 1 Introduction

1.1 Background

A multirotor is a type of vertical take-off-and-landing unmanned aerial vehicle that has enormous potential due to its agility, mobility, lightness, and maneuverability. These advantages have resulted in multirotors being widely utilized in various fields, including cooperative load transportation [1], search and rescue [2], and military surveillance [3].

Numerous studies have investigated how to control a multirotor, including using linear control methods such as PID control and feedback linearization [4], [5], and [6] and feedback linearization method and adaptive sliding mode control method based on the Lyapunov stability theory [7], [8], [9], and [10]. A geometric tracking control method that calculated the attitude and angular velocity tracking error on $\mathrm{SO}(3)$ was developed in [11]. This method avoided the singularities of Euler angles and guaranteed the exponential stability through Lyapunov stability theory when the initial attitude error is less than $180°$.

1.2 Motivation

Since the dynamics of the multirotor is highly nonlinear, it is important to design a nonlinear controller rather than using a linear controller. Knowledge of the geometric and inertia parameters is essential to achieving good control performance. The mass of the system is an important parameter influencing the translational dynamics. The moment of inertia, which represents the tendency of an object to resist changes in the angular velocity, is important for the attitude control of multirotors. Thus, acquiring knowledge and information about both kinds of inertia is the primary task before designing the controller.

1.3 Related Works

1.3.1 Estimate the Mass of the Multirotor

Several methods have been used to estimate the mass of a multirotor, such as the linear least-squares method and an extended Kalman filter. [12] estimated the mass of the whole system including the multirotor, grasper, and payload using a linear least-squares method in a multirotor used for aerial grasping. In order to deal with the situation of grasping a different pay-

load, [12] formulated the dynamics model considering the mass change of the multirotor system. In [13], the authors designed an estimator that estimated the mass of the multirotor using only inertia measurements and pilot commands. They derived a dynamics model that considered the relation between roll rate and lateral acceleration. Furthermore, those authors compared the performances of several methods for estimating the mass of the multirotor, including least-squares estimation, an extended Kalman filter, and an instrumental variable method. [14] presented two methods for estimating parameters of a multirotor that included the mass and the reformulated moment of inertia. The smooth variable structure filter method with information about chattering signal and the recursive least squares were applied to estimate the parameters , and the accuracies of estimation of these two estimation methods were compared. The authors also conducted simulations that including sensor noise in order to mimic the real flight. However, the algorithms in [12], [13], and [14] were developed using Euler angles, and were limited by the gimbal lock phenomenon.

1.3.2 Estimate the Moment of Inertia of the Multirotor

There are several methods available for obtaining the moment of inertia during setup, such as tabulation method in [15] and [16], and CAD-based method in [17] and [18]. In tabulation method involves disassembling the multirotor model into simple geometrical objects such as cross-beam, cylinder, and boxes elements. The body-fixed frame is considered to have a cross-beam geometry, while motors and propellers are regarded as cylinders with different dimensions. The total moment of inertia of the multirotor is calculated by combining the inertia contribution of each component and using the parallel-axis theorem. However, the complicated real structure of a multirotor might be oversimplified by using these simple elements.

In the CAD-based method, a model of the multirotor is constructed using computer software. This approach means that the model is not restricted to elements with simple geometries, meaning that the constructed multirotor model can have greater complexity and a more-accurate structure. Moreover, all parameters related to the dynamics and control of the multirotor are available in the software. However, the parameters may differ between the simulations and the real structure, and also due to imperfections associated with the manufacturing and assembly processes.

[19] proposed a method for estimating the moment of inertia directly from flight data. The method modified the Newton-Euler equation of motion for the rotational dynamics to derive a

linear and algebraic model. The flight data were used to solve the unknown parameters by taking numerically time derivative of the gyroscope signal, which is vulnerable to noises. Moreover, calculating the inverse of the matrix is too complicated to be performed on the on-board computers. Needing a high-performance flight controller for recording the flight data also increases the cost of a multirotor.

A frequency-domain approach for estimating the moment of inertia [20] can be applied equally to full-size helicopters and small multirotors. The dynamics of the system after linearization is fully described by frequency-response approaches, but the stability of the linearized system is only guaranteed around the equilibrium point. The performance of the controller may be impaired by nonlinear dynamics of the real physical system. Moreover, the model in [20] was derived for the hovering condition and the motion of the system is restricted to one axis at a time, whereas multirotors are usually required to follow a desired trajectory.

The methods for estimating the moment of inertia mentioned above are based on offline analysis. [21] proposed an approach for accurately estimating physical parameters based on the maximum-likelihood estimation. This approach reflects the uncertainty of the measurement implicit in the probability distribution. However, collecting flight data may increases the computational complexity of the on-board computer.

It is not possible to determine the variations in parameters when the structure of a multirotor changes in real time. Such parameter variations could occur when a payload is attached to a multirotor during a flight. This kinds of problems were addressed in [22] by designing a real-time, on-board estimator for estimating the geometric and inertia parameters of a multirotor. This estimator is able to re-estimate the parameters as they change during the flight time. Nevertheless, that could only estimate unbiased states and parameters when the system was locally weakly observable.

An adaptive control method based on Lyapunov stability theory was developed to design a controller with unknown system parameters. [23], [24], and [25] implemented this control method on a multirotor for which the moment of inertia was unknown.

1.4 Contributions

The present study has developed an integral concurrent learning (ICL) control method that can simultaneously stabilize the multirotor and estimate the moment of inertia. By combining the controller architecture in [11] and [26], a concurrent learning method has been developed for

estimating the system parameters. Not only is the control objective of attitude tracking achieved, but also the unknown moments of inertia converge to close to their true values.

The main contributions of this study are summarized as follows:

1. This is the first study to develop a method of ICL for asymptotically estimating the mass and moment of inertia of a multirotor.
2. The dynamics of the multirotor is globally defined, and so the developed ICL controller can perform asymptotic tracking and parameter estimation.
3. The developed ICL controller can estimate the system parameters online, requiring less human intervention, which is very useful in the application of package delivery in which the mass and moment of inertia of the overall system is unknown.
4. The developed ICL controller can be applied to multirotors with different numbers of axes and ensures asymptotic tracking.

Chapter 2 Problem Formulation

2.1 Dynamics of the Multirotor

The multirotor is described by both translational and rotational dynamics. The translational dynamics considers forces such as the effects of gravity, thrusts, and external forces, whereas the rotational dynamics takes the moment of the control input, rotational speed, and moment of inertia into account. The dynamics of the multirotor is formulated as

$$\dot{x} = v, \tag{1}$$

$$m\dot{v} = mge_3 - fRe_3, \tag{2}$$

$$\dot{R} = R\hat{\Omega}, \tag{3}$$

$$J\dot{\Omega} + \Omega \times J\Omega = M, \tag{4}$$

where $x, v \in \mathbb{R}^3$ represent the position and velocity in the inertial frame, respectively, and $f \in \mathbb{R}$ and $M \in \mathbb{R}^3$ are net thrust and moment control inputs, respectively, in the body-fixed frame. $R \in \mathrm{SO}(3)$ is the rotation matrix from the body-fixed frame to the inertial frame, as shown in Fig. 1. m and $g \in \mathbb{R}$ are the unknown mass of the multirotor and gravity, respectively, e_3 is an unit vector defined as $e_3 = [0, 0, 1]^T \in \mathbb{R}^3$, $\Omega = \begin{bmatrix} \Omega_1 & \Omega_2 & \Omega_3 \end{bmatrix}^T$ is defined as the angular velocity of the multirotor, $\dot{\Omega}$ is the angular acceleration of the multirotor, and $\boldsymbol{J} \in \mathbb{R}^{3\times3}$ is the unknown inertia matrix of the multirotor defined as

$$\boldsymbol{J} = \begin{bmatrix} J_{xx} & 0 & 0 \\ 0 & J_{yy} & 0 \\ 0 & 0 & J_{zz} \end{bmatrix}, \tag{5}$$

which is estimated in the subsequent analysis.

The notations of the symbols are presented in Table 1. The multirotors can have n rotors, where $n \in \{4, 6, 8, \ldots\}$, and the only difference between the rotors is in the allocation matrix. In a four-rotor multirotor, the first and third propellers rotate clockwise, and the second and fourth propellers rotate counterclockwise. The total moment generated by the propellers in the

body-fixed frame is defined as

$$M \triangleq \begin{bmatrix} M_1 \\ M_2 \\ M_3 \end{bmatrix} = \begin{bmatrix} d\,(f_4 - f_2) \\ d\,(f_1 - f_3) \\ c_{\tau f}\,(-f_1 + f_2 - f_3 + f_4) \end{bmatrix},$$

where f_i is the thrust generated by the i^{th} propeller along the $-\vec{Z}_B$ axis and can be obtained from (6) given f and M, $d > 0$ is the distance between the center of mass and the center of a propeller, and $c_{\tau f} > 0$ is a constant parameter of the propeller. The relation between f, M, and f_i can be expressed through the allocation matrix as

$$\begin{bmatrix} f \\ M_1 \\ M_2 \\ M_3 \end{bmatrix} = \begin{bmatrix} 1 & 1 & 1 & 1 \\ 0 & -d & 0 & d \\ d & 0 & -d & 0 \\ -c_{\tau f} & c_{\tau f} & -c_{\tau f} & c_{\tau f} \end{bmatrix} \begin{bmatrix} f_1 \\ f_2 \\ f_3 \\ f_4 \end{bmatrix}. \tag{6}$$

For a six-rotor multirotor, (6) can be modified as

$$M = \begin{bmatrix} d\left(\frac{1}{2} \cdot (f_1 + f_3 - f_4 - f_6) + (f_2 - f_5)\right) \\ d \cdot \frac{\sqrt{3}}{2}\,(f_3 + f_4 - f_1 - f_6) \\ c_{\tau f}\,(-f_1 + f_2 - f_3 + f_4 - f_5 + f_6) \end{bmatrix},$$

which changes the allocation matrix of the six-rotor multirotor to

$$\begin{bmatrix} 1 & 1 & 1 & 1 & 1 & 1 \\ \frac{d}{2} & d & \frac{d}{2} & -\frac{d}{2} & -d & -\frac{d}{2} \\ -\frac{\sqrt{3}d}{2} & 0 & \frac{\sqrt{3}d}{2} & \frac{\sqrt{3}d}{2} & 0 & -\frac{\sqrt{3}d}{2} \\ -c_{\tau f} & c_{\tau f} & -c_{\tau f} & c_{\tau f} & -c_{\tau f} & c_{\tau f} \end{bmatrix}. \tag{7}$$

Table 1: Definition of symbols

Symbol	Description
$x \in \mathbb{R}^3$	multirotor position in the inertial frame
$v \in \mathbb{R}^3$	multirotor velocity in the inertial frame
$R \in \mathrm{SO}(3)$	rotation matrix from the body-fixed frame to the inertial frame
$\Omega \in \mathbb{R}^3$	angular velocity in the body-fixed frame
$f \in \mathbb{R}$	net thrust in the body-fixed frame
$f_i \in \mathbb{R}$	thrust generated by the i^{th} propeller
$M \in \mathbb{R}^3$	total moment in the body-fixed frame
$m \in \mathbb{R}$	mass of the multirotor, which is assumed to be an unknown constant
$d \in \mathbb{R}$	distance between the center of mass and the center of the propeller
$J \in \mathbb{R}^{3\times 3}$	inertia matrix, which is assumed to be an unknown constant matrix

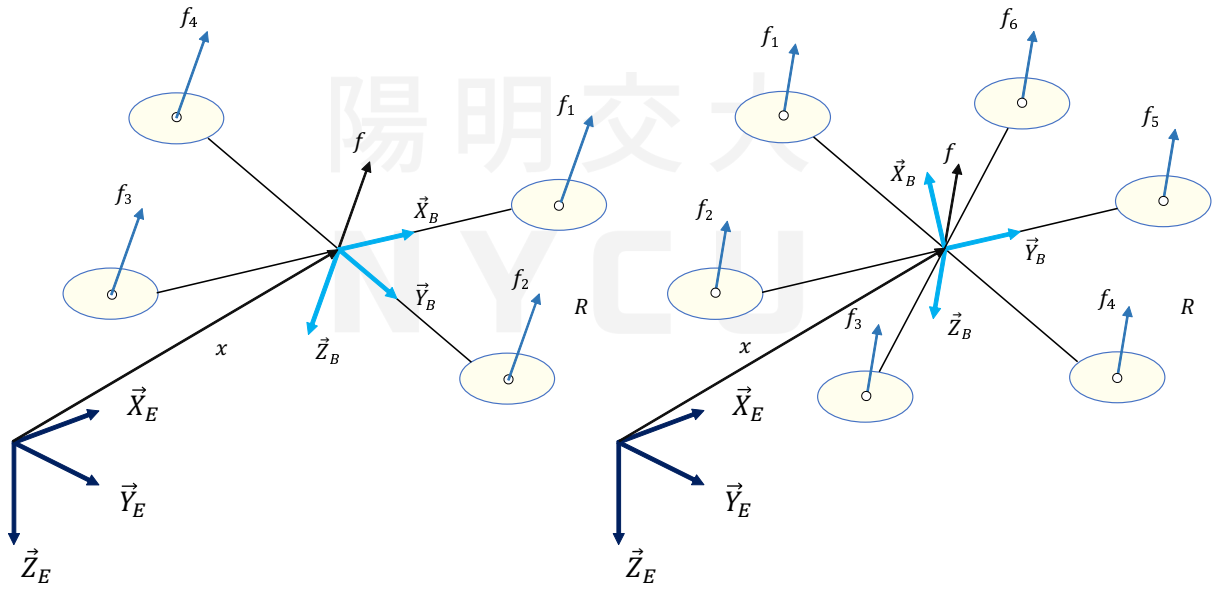

Figure 1: Coordinate systems of four-rotor and six-rotor multirotors.

As shown in Fig. 1, the inertial frame and body-fixed frame are defined as $\left\{ \vec{X}_E, \ \vec{Y}_E, \ \vec{Z}_E \right\}$ and $\left\{ \vec{X}_B, \ \vec{Y}_B, \ \vec{Z}_B \right\}$, respectively.

Remark 1. Note that the dynamics defined by (1) – (4) can be extended to multirotors with different numbers of axes by replacing the allocation matrix.

2.2 Tracking Errors and Estimate Errors

Given a desired trajectory $x_d \in \mathbb{R}^3$, the position and velocity tracking errors are defined as

$$e_x \triangleq x - x_d, \tag{8}$$

$$e_v \triangleq v - v_d, \tag{9}$$

where $v_d \triangleq \dot{x}_d \in \mathbb{R}^3$ is the desired velocity. To address the rotational dynamics in the subsequent analysis, the attitude error function on $\mathrm{SO}(3)$, the attitude tracking error, and the angular velocity tracking error are defined as

$$\Psi(R, R_d) \triangleq \frac{1}{2}\mathrm{tr}\left[I - R_d^T R\right], \tag{10}$$

$$e_R \triangleq \frac{1}{2}\left(R_d^T R - R^T R_d\right)^\vee, \tag{11}$$

$$e_\Omega \triangleq \Omega - R^T R_d \Omega_d, \tag{12}$$

where $R_d = \left[\vec{X}_{B_d}, \vec{Y}_{B_d}, \vec{Z}_{B_d}\right] \in \mathrm{SO}(3)$ is the desired attitude for the multirotor, and $(\check{\cdot}) : \mathrm{SO}(3) \to \mathbb{R}^3$ is the vee map. Angular velocity $\Omega_d = \left(R_d^T \dot{R}_d\right)^\vee$ can be obtained from the rotational dynamics of the multirotor as described in (3). The estimate error of the mass is defined as

$$\tilde{\theta}_m \triangleq \theta_m - \hat{\theta}_m, \tag{13}$$

where θ_m is defined as

$$\theta_m \triangleq m \in \mathbb{R}, \tag{14}$$

and $\hat{\theta}_m$ is the estimate of θ_m and is updated by $\dot{\hat{\theta}}_m$ as described below.

The moment of inertia defined in (5) is reshaped to a constant column vector θ_J defined as

$$\theta_J = \begin{bmatrix} J_{xx}, & J_{yy}, & J_{zz} \end{bmatrix}^T, \tag{15}$$

where the elements in θ_J are unknown constants to be estimated during flight. The estimate error of the moment of inertia is defined as

$$\tilde{\theta}_J \triangleq \theta_J - \hat{\theta}_J, \tag{16}$$

where $\hat{\theta}_J$ is the estimate of θ_J and is updated by $\dot{\hat{\theta}}_J$ as described below.

2.3 Control Objectives

The flight controller is designed for the multirotor to track a desired trajectory x_d and desired yaw direction $\vec{X}_{B_d}$, and also estimate the unknown mass and moment of inertia of the multirotor (θ_m and θ_J) during flight. These control objectives are described as

$$\begin{cases} e_x & \to 0 \\ e_v & \to 0 \\ e_R & \to 0 \\ e_\Omega & \to 0 \\ \tilde{\theta}_m & \to 0 \\ \tilde{\theta}_J & \to 0 \end{cases} \quad as \quad t \to \infty. \tag{17}$$

Chapter 3 Controller Design

To ensure that the multirotor achieves the control objectives defined in (17) as well as estimate the unknown mass and moment of inertia, translational and rotational controllers f and M are designed using an ICL-based update law, as described below.

3.1 Translational Controller for the Multirotor

Let the translational controller be designed as

$$f = (k_x e_x + k_v e_v + Y_m \hat{\theta}_m) \cdot Re_{3,} \tag{18}$$

where k_x, k_v are positive control gains, and Y_m is a regression matrix defined as $Y_m : \mathbb{R}^n \times [0, \infty) \to \mathbb{R}^{n \times m}$

$$Y_m = \begin{bmatrix} -\ddot{x}_{d_1} \\ -\ddot{x}_{d_2} \\ g - \ddot{x}_{d_3} \end{bmatrix}, \tag{19}$$

where $\ddot{x}_{d_1}$, $\ddot{x}_{d_2}$, and $\ddot{x}_{d_3} \in \mathbb{R}$ are the elements of the acceleration of the desired trajectory of the multirotor $\ddot{x}_d$. Y_m comprising gravity and the command acceleration is bounded by a positive constant $\bar{Y}_m \in \mathbb{R}_{>0}$:

$$\|Y_m\| < \bar{Y}_m. \tag{20}$$

Remark 2. Note that the controller designed in (18) is the net thrust obtained by projecting the force control input $\vec{f}$ into e_3 on the body frame:

$$\vec{f} = k_x e_x + k_v e_v + Y_m \hat{\theta}_m. \tag{21}$$

The translational dynamics of the multirotors defined in (2) can be rewritten as

$$fRe_3 = mge_3 - m\dot{v}, \tag{22}$$

which can be linearly parameterized to separate the known and unknown parameters as

$$fRe_3 = Y_m^{cl} \theta_m, \tag{23}$$

where $Y_m^{cl} : \mathbb{R}^n \times [0, \infty) \to \mathbb{R}^{n \times m}$ is a regression matrix defined as

$$Y_m^{cl} = \begin{bmatrix} -\ddot{x}_1 \\ -\ddot{x}_2 \\ g - \ddot{x}_3 \end{bmatrix}, \tag{24}$$

and $\hat{\theta}_m$ estimates θ_m using the ICL-based update law

$$\begin{aligned} \dot{\hat{\theta}}_m =& \text{proj}\left(\Gamma_m Y_m^T \left(e_v + C_1 e_x\right)\right) \\ &+ \text{proj}\left(k_m^{cl} \Gamma_m \sum_{j=1}^{N_m} \left(y_m^{cl}\left(t_j\right)\right)^T \left(F - y_m^{cl}\left(t_j\right) \hat{\theta}_m\left(t_j\right)\right)\right), \end{aligned} \tag{25}$$

where Γ_m, $k_m^{cl}, C_1 \in \mathbb{R}_{>0}$ are positive control gains, $t_j \in [0, t]$ is the time between the initial time and the current time, and $N_m \in \mathbb{Z}^+$ is a positive constant that characterizes the amount of data used for the ICL controller. The proj $(\cdot)$ operation is inspired by [27] and it ensures that $\hat{\theta}_m$ is upper bounded by a prescribed positive constant $\bar{\hat{\theta}}_m$ as

$$\left\|\hat{\theta}_m\right\| < \bar{\hat{\theta}}_m. \tag{26}$$

In (25), F and y_m^{cl} are defined as

$$F(t) \triangleq \begin{cases} 0_{n\times 1} & t \in [0, \triangle t] \\ \int_{t-\triangle t}^{t} f Re_3\left(\tau\right) d\tau & t > \triangle t \end{cases}, \tag{27}$$

$$y_m^{cl}(t) \triangleq \begin{cases} 0_{n\times 1} & t \in [0, \triangle t] \\ \int_{t-\triangle t}^{t} Y_m^{cl}(\tau) d\tau & t > \triangle t \end{cases}, \tag{28}$$

where $\triangle t \in \mathbb{R}$ is the time interval of integration.

Proposition 1. *$\dot{\hat{\theta}}_m$ defined in (25) is equivalent to*

$$\begin{aligned} \dot{\hat{\theta}}_m =& \textit{proj}\left(\Gamma_m Y_m^T \left(e_v + C_1 e_x\right)\right) \\ &+ \textit{proj}\left(k_m^{cl} \Gamma_m \mathcal{G}_m \tilde{\theta}_m\right). \end{aligned} \tag{29}$$

Proof. Integrating both sides of (23) yields

$$\int_{t-\triangle t}^{t} fRe_3\left(\tau\right) d\tau = \int_{t-\triangle t}^{t} Y_m^{cl}(\tau)\theta_m d\tau, \tag{30}$$

where $\theta_m \in \mathbb{R}$ represents the constant unknown mass, and $\forall t > \triangle t$. Using the fundamental theorem of calculus and the definitions in (27) and (28) yields

$$\int fRe_3(\tau) \mid_{\tau=t} - \int fRe_3(\tau) \mid_{\tau=t-\triangle t} = y_m^{cl}(t)\theta_m. \tag{31}$$

Substituting (31) into (25) yields (29), wherewhere $\mathcal{G}_m \triangleq \sum_{j=1}^{N_m} \left(y_{m,j}^{cl}\right)^T y_{m,j}^{cl}$. □

Remark 3. The Y_m^{cl} defined in (24) is not implementable since it includes acceleration terms $\ddot{x}_1$, $\ddot{x}_2$, and $\ddot{x}_3$, which are not measurable. However, by integrating Y_m^{cl} to be y_m^{cl} as defined in (28), y_m^{cl} becomes implementable since v_1, v_2, and v_3 are available.

3.2 Rotational Controller for the Multirotor

The subsequent analysis is facilitated by making the following assumption:

$$\left\| -k_x e_x - k_v e_v - Y_m \hat{\theta}_m \right\| \neq 0, \tag{32}$$

which is similar to [11].

Let the rotational controller be designed as

$$M = -k_R e_R - k_\Omega e_\Omega - Y_J \hat{\theta}_J, \tag{33}$$

where k_R, k_Ω are positive control gains, and $Y_J : \mathbb{R}^n \times [0, \infty) \rightarrow \mathbb{R}^{n \times m}$ is a regression matrix defined as

$$Y_J = \begin{bmatrix} \overline{\Omega}_1 & \Omega_2 \cdot \Omega_3 & -\Omega_2 \cdot \Omega_3 \\ -\Omega_1 \cdot \Omega_3 & \overline{\Omega}_2 & \Omega_1 \cdot \Omega_3 \\ \Omega_1 \cdot \Omega_2 & -\Omega_1 \cdot \Omega_2 & \overline{\Omega}_3 \end{bmatrix}, \tag{34}$$

where $\overline{\Omega}_1$, $\overline{\Omega}_2$, and $\overline{\Omega}_3 \in \mathbb{R}$ are the elements of $\overline{\Omega} \in \mathbb{R}^3$ defined as

$$\overline{\Omega} \triangleq \begin{bmatrix} \overline{\Omega}_1 \\ \overline{\Omega}_2 \\ \overline{\Omega}_3 \end{bmatrix} = \hat{\Omega} R^T R_d \Omega_d - R^T R_d \dot{\Omega}_d, \tag{35}$$

where $R_d = \left[\vec{X}_{B_d}, \vec{Y}_{B_d}, \vec{Z}_{B_d}\right] \in \mathrm{SO}(3)$ and

$$\vec{Z}_{B_d} = -\frac{-k_x e_x - k_v e_v - Y_m \hat{\theta}_m}{\left\| -k_x e_x - k_v e_v - Y_m \hat{\theta}_m \right\|} \tag{36}$$

designed using an approach similar to that adopted in [11], are the desired attitude and the z-axis of the body-fixed frame of the multirotor, respectively, and $\vec{Z}_{B_d}$ exists based on (32). Based on the definitions of Y_m, θ_m, (20), and (26), the following inequalities are satisfied:

$$\| -Y_m \theta_m \| < \| Y_m \| \, \| \theta_m \| < \bar{Y}_m \bar{\hat{\theta}}_m < B, \tag{37}$$

where $B \in \mathbb{R}_{>0}$ is a positive constant.

To facilitate the following analysis, the rotational dynamics of the multirotors defined in (4) can be further linearly parameterized as

$$M = Y_J^{cl} \theta_J, \tag{38}$$

where $Y_J^{cl} : \mathbb{R}^n \times [0, \infty) \to \mathbb{R}^{n \times m}$ is a regression matrix defined as

$$Y_J^{cl} = \begin{bmatrix} \dot{\Omega}_1 & -\Omega_2 \cdot \Omega_3 & \Omega_2 \cdot \Omega_3 \\ \Omega_1 \cdot \Omega_3 & \dot{\Omega}_2 & -\Omega_1 \cdot \Omega_3 \\ -\Omega_1 \cdot \Omega_2 & \Omega_1 \cdot \Omega_2 & \dot{\Omega}_3 \end{bmatrix}, \tag{39}$$

and θ_J is the unknown constants to be estimated according to (15).

The last term in (33), $\hat{\theta}_J$, is updated to estimate θ_J by applying the ICL-based update law:

$$\dot{\hat{\theta}}_J(t) \triangleq \Gamma_J Y_J^T (e_\Omega + C_2 e_R) + k_J^{cl} \Gamma_J \sum_{j=1}^{N_J} \left(y_J^{cl}(t_j)\right)^T (\overline{M}(t_j) - y_J^{cl}(t_j)\hat{\theta}_J), \tag{40}$$

where $k_J^{cl} \in \mathbb{R}$ is the control gain, $C_2 \in \mathbb{R}$ is a positive constant, $N_J \in \mathbb{Z}^+$ is a positive constant that characterizes the number of data used for concurrent learning, $\Gamma_J \in \mathbb{R}^{m\times m}$ is a constant gain matrix, and y_J^{cl} and $\overline{M}$ are defined as

$$y_J^{cl}(t) \triangleq \begin{cases} 0_{n\times m} & t \in [0, \triangle t] \\ \int_{t-\triangle t}^{t} Y_J^{cl}(\Omega(\tau), \tau) d\tau & t > \triangle t \end{cases}, \tag{41}$$

$$\overline{M}(t) \triangleq \begin{cases} 0_{n\times 1} & t \in [0, \triangle t] \\ \int_{t-\triangle t}^{t} M(\tau) d\tau & t > \triangle t \end{cases}. \tag{42}$$

Proposition 2. *$\dot{\hat{\theta}}_J$ defined in (40) is equivalent to*

$$\dot{\hat{\theta}}_J = \Gamma_J Y_J^T (e_\Omega + C_2 e_R) + k_J^{cl} \Gamma_J \mathcal{G}_J \tilde{\theta}_J. \tag{43}$$

Proof. Integrating both sides of (38) yields

$$\int_{t-\triangle t}^{t} M(\tau) d\tau = \int_{t-\triangle t}^{t} Y_J^{cl}(\Omega, \tau)\theta_J d\tau.$$

Using the fundamental theorem of calculus and the definitions in (42) and (41) yields

$$\int M(\tau) \mid_{\tau=t} - \int M(\tau) \mid_{\tau=t-\triangle t} = y_J^{cl}(t)\theta_J. \tag{44}$$

Substituting (44) into (40) yields (43), where $\mathcal{G}_J \triangleq \sum_{j=1}^{N_J} \left(y_{J,j}^{cl}\right)^T y_{J,j}^{cl}$ and $\tilde{\theta}_J$ is the estimate error defined in (16). □

Remark 4. The Y_J^{cl} defined in (39) is not implementable since it includes angular acceleration terms $\dot{\Omega}_1$, $\dot{\Omega}_2$, and $\dot{\Omega}_3$, which are not measurable. However, by integrating Y_J^{cl} to be y_J^{cl} as defined in (41), y_J^{cl} becomes implementable since Ω_1, Ω_2, and Ω_3 are available.

A block diagram of the ICL controller is depicted in Fig. 2.

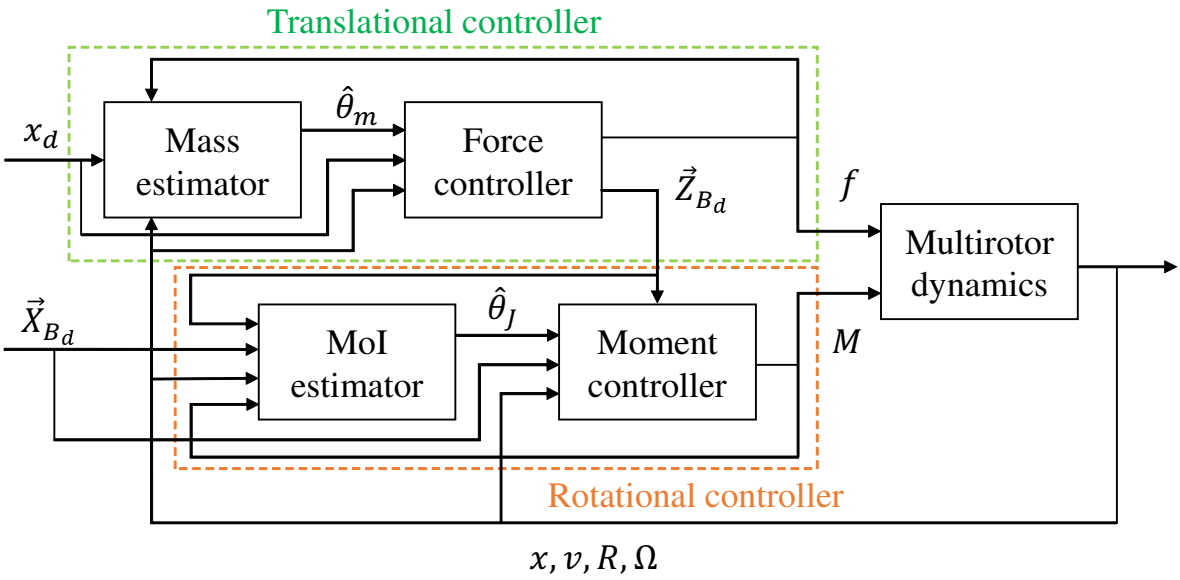

Figure 2: Control architecture of the ICL controller. MoI, moment of inertia.

3.3 Closed-Loop Error System

To facilitate the stability analysis presented in Chapter 4, the closed-loop error systems of rotational and translational dynamics are derived in this section.

3.3.1 Translational Dynamics

Taking the time derivative of (9) and substituting the translational dynamics of the multirotor defined in (2) yields

$$\begin{aligned} m\dot{e}_v =& mge_3 - fRe_3 - m\ddot{x}_d \\ =& Y_m\theta_m - fRe_3, \end{aligned} \tag{45}$$

where Y_m and θ_m are defined in (19) and (14). By substituting the force control (18) into (45), and adding and subtracting $\frac{f}{e_3^T R_d^T R e_3} R_d e_3$ to the right-hand side of (45) yields the closed-loop translation dynamics of the multirotor as

$$m\dot{e}_v = -k_x e_x - k_v e_v + Y_m\tilde{\theta}_m - X, \tag{46}$$

where $X \in \mathbb{R}^3$ is defined as

$$X = \frac{f}{e_3^T R_d^T R e_3}\Big(\left(e_3^T R_d^T R e_3\right) R e_3 - R_d e_3 \Big).$$

3.3.2 Rotational Dynamics

Taking the time derivative of error dynamics e_R and e_Ω defined in (11) and (12) yields

$$\begin{aligned} \dot{e}_R &= \frac{1}{2}(R_d^T R \hat{e}_\Omega + \hat{e}_\Omega R^T R_d)^\vee \\ &= C(R_d^T R) e_\Omega, \end{aligned} \tag{47}$$

$$\begin{aligned} \dot{e}_\Omega &= \dot{\Omega} + (\hat{\Omega} R^T R_d \Omega_d - R^T R_d \dot{\Omega}_d) \\ &= \dot{\Omega} + \overline{\Omega}, \end{aligned} \tag{48}$$

where $C(R_d^T R)$ is defined as

$$C(R_d^T R) \triangleq \frac{1}{2}(\text{tr}[R^T R_d] I - R^T R_d). \tag{49}$$

Multiplying (48) by J and substituting the rotation dynamics of the multirotor (4) into (48) yields

$$J\dot{e}_\Omega = M + Y_J \theta_J, \tag{50}$$

where $Y_J \theta_J$ is defined as

$$Y_J \theta_J = J\overline{\Omega} - \Omega \times J\Omega, \tag{51}$$

where J, θ_J, and Y_J are defined in (5), (15), and (34), respectively. Substituting the rotational control input (33) into (50) yields

$$J\dot{e}_\Omega = -k_R e_R - k_\Omega e_\Omega + Y_J \tilde{\theta}_J. \tag{52}$$

Chapter 4 Stability Analysis

The stability analysis of this control algorithm can be divided into two parts: rotational and translational. Lyapunov functions V_1 and V_2 are designed to prove the stability of the translational and rotational dynamics, respectively. The stability of the overall system is then proven by using $V = V_1 + V_2$ [28].

4.1 Stability Analysis of the Rotational Dynamics

Theorem 1. *The controller designed in (33) can ensure e_R and e_Ω achieve exponential stability and $\Psi\left(R\left(t\right), R_d\left(t\right)\right)$ and ψ_2 defined in (10) and (61) satisfy*

$$\Psi\left(R\left(t\right), R_d\left(t\right)\right) \leq \psi_2 < 2 \tag{53}$$

provided that the following conditions are satisfied

$$\Psi\left(R\left(0\right), R_d\left(0\right)\right) < 2 \tag{54}$$

$$\left\|e_\Omega\left(0\right)\right\|^2 < \frac{2}{\lambda_{\max}\left(J\right)} k_R \left(2 - \Psi\left(R\left(0\right), R_d\left(0\right)\right)\right). \tag{55}$$

$$C_2 < \min\Big\{ \frac{k_\Omega}{\lambda_{\max}\left(J\right)}, \frac{4k_\Omega k_R}{k_\Omega^2 + 4k_R\lambda_{\max}\left(J\right)}, \sqrt{\frac{k_R\lambda_{\min}\left(J\right)}{\lambda_{\max}\left(J\right)^2}} \Big\}, \tag{56}$$

where C_2 is a positive constant.

Proof. Let V_2 be defined as

$$V_2 = \frac{1}{2} e_\Omega \cdot J e_\Omega + k_R \Psi(R, R_d) + J C_2 e_R \cdot e_\Omega + \frac{1}{2} \tilde{\theta}_J^T \Gamma_J^{-1} \tilde{\theta}_J, \tag{57}$$

which can be lower and upper bounded by

$$z_2^T M_{21} z_2 + \frac{1}{2} \tilde{\theta}_J^T \Gamma_J^{-1} \tilde{\theta}_J \leq V_2 \leq z_2^T M_{22} z_2 + \frac{1}{2} \tilde{\theta}_J^T \Gamma_J^{-1} \tilde{\theta}_J, \tag{58}$$

where $z_2 \triangleq \left[\begin{array}{cc} \|e_R\|, & \|e_\Omega\| \end{array} \right]^T$

$$M_{21} = \frac{1}{2} \left[\begin{array}{cc} k_R & -C_2 \lambda_{\max}(J) \\ -C_2 \lambda_{\max}(J) & \lambda_{\min}(J) \end{array} \right], \tag{59}$$

$$M_{22} = \frac{1}{2} \left[\begin{array}{cc} \frac{2k_R}{2-\psi_2} & C_2 \lambda_{\max}(J) \\ C_2 \lambda_{\max}(J) & \lambda_{\max}(J) \end{array} \right], \tag{60}$$

where $\psi_2 \in \mathbb{R}$ is defined as

$$\psi_2 = \frac{1}{k_R} \left[\frac{1}{2} e_\Omega(0) \cdot J e_\Omega(0) + k_R \Psi(R(0), R_d(0)) \right]. \tag{61}$$

Taking the time derivative of V_2 yields

$$\begin{aligned} \dot{V}_2 =& e_\Omega \cdot J \dot{e}_\Omega - \frac{1}{2} k_R \text{tr}[-\hat{\Omega}_d R_d^T R + R_d^T R \hat{\Omega}] \\ &+ J C_2 \dot{e}_R \cdot e_\Omega + J C_2 \dot{e}_\Omega \cdot e_R \\ &+ \tilde{\theta}_J^T \Gamma_J^{-1} \dot{\tilde{\theta}}_J \\ =& e_\Omega \cdot J \dot{e}_\Omega - \frac{1}{2} k_R \text{tr}[R_d^T R \hat{e}_\Omega] \\ &+ J C_2 \dot{e}_R \cdot e_\Omega + J C_2 \dot{e}_\Omega \cdot e_R \\ &+ \tilde{\theta}_J^T \Gamma_J^{-1} \dot{\tilde{\theta}}_J. \end{aligned} \tag{62}$$

The second and fifth terms of (62) can be written as

$$\begin{aligned} \text{tr}[R_d^T R \hat{e}_\Omega] &= \frac{1}{2} \text{tr}[R_d^T R \hat{e}_\Omega - \hat{e}_\Omega R^T R_d] \\ &= \frac{1}{2} \text{tr}[\hat{e}_\Omega (R_d^T R - R^T R_d)] = \text{tr}[\hat{e}_\Omega \hat{e}_R] \\ &= -2 e_R e_\Omega. \end{aligned} \tag{63}$$

$$\dot{\tilde{\theta}}_J = -\dot{\hat{\theta}}_J. \tag{64}$$

Based on (47), (52), (63), and (64), (62) can be written as

$$\begin{aligned} \dot{V}_2 =& (e_\Omega + C_2 e_R) \cdot (-k_R e_R - k_\Omega e_\Omega + Y_J \tilde{\theta}_J) + k_R e_\Omega \cdot e_R \\ &+ J C_2 C (R_d^T R) e_\Omega \cdot e_\Omega - \tilde{\theta}_J^T \Gamma_J^{-1} \dot{\hat{\theta}}_J. \end{aligned} \tag{65}$$

Since $C(R_d^T R)$ defined in (49) can be bounded as $\left\|C(R_d^T R)\right\| \leq 1$, substituting the equivalent ICL-based update law in Proposition 2 into (65) yields

$$\dot{V}_2 \leq -z_2^T W_2 z_2 - k_J^{cl} \tilde{\theta}_J^T \mathcal{G}_J \tilde{\theta}_J, \tag{66}$$

where W_2 is defined as

$$W_2 = \begin{bmatrix} C_2 k_R & -\frac{C_2 k_\Omega}{2} \\ -\frac{C_2 k_\Omega}{2} & k_\Omega - C_2 \lambda_{\max}(J) \end{bmatrix}. \tag{67}$$

To facilitate the subsequent analysis, the analysis is divided into two steps.

Step 1: to prove (53). Supposing that $C_2 = 0$, e_R will drop from (57), and (57) and (66) can be rewritten as

$$\begin{aligned} V_2 \mid_{C_2=0} &= \frac{1}{2} e_\Omega \cdot J e_\Omega + k_R \Psi(R, R_d) + \frac{1}{2} \tilde{\theta}_J^T \Gamma_J^{-1} \tilde{\theta}_J, \\ \dot{V}_2 \mid_{C_2=0} &\leq -k_\Omega \left\|e_\Omega\right\|^2 - k_J^{cl} \tilde{\theta}_J^T \mathcal{G}_J \tilde{\theta}_J, \end{aligned}$$

which implies that $V_2 \mid_{C_2=0}$ is nonincreasing. Therefore, given the initial conditions (54) and (55), the attitude error function can be bounded as

$$\begin{aligned} &k_R \Psi\left(R\left(t\right), R_d\left(t\right)\right) + \frac{1}{2} \tilde{\theta}_J^T \Gamma_J^{-1} \tilde{\theta}_J \leq V_2 \mid_{C_2=0} (t) \leq \\ &V_2 \mid_{C_2=0} (0) < 2k_R + \frac{1}{2} \tilde{\theta}_J^T \Gamma_J^{-1} \tilde{\theta}_J, \end{aligned} \tag{68}$$

which guarantees that

$$\Psi\left(R\left(t\right), R_d\left(t\right)\right) \leq \psi_2 < 2,$$

which proves (53) and ensures the element $\frac{2k_R}{2-\psi_2}$ defined in (60) is positive. Therefore, $R\left(t\right)$ always lies in the sublevel set $L_2 \triangleq \{R \in \mathrm{SO}(3) \mid \Psi\left(R, R_d\right) < 2\}$. Within sublevel set L_2, the attitude error function is positive definite:

$$\frac{1}{2} \left\|e_R\right\|^2 \leq \Psi \leq \frac{1}{2 - \psi_2} \left\|e_R\right\|^2.$$

Step 2: To prove e_R and e_Ω achieve exponential stability, the matrices M_{21}, M_{22}, and W_2 defined in (59), (60), and (67) are positive definite by selecting C_2 to satisfy (56). Since V_2 is positive definite and $\dot{V}_2$ is negative definite based on (58) and (67), Theorem 1 is proven. □

Remark 5. Although J in (56) is unknown, its maximal and minimal eigenvalues can be obtained from best guesses.

4.2 Stability Analysis of the Translational Dynamics

To facilitate the subsequent analysis, the following proposition id developed.

Proposition 3. *ψ_1 defined in (72) satisfies*

$$\Psi\left(R\left(t\right), R_d\left(t\right)\right) \leq \psi_1 < 1. \tag{69}$$

provided that the initial conditions are satisfied

$$\Psi\left(R\left(0\right), R_d\left(0\right)\right) < 1, \tag{70}$$

$$\left\|e_\Omega\left(0\right)\right\|^2 < \frac{2}{\lambda_{\max}\left(J\right)} k_R\left(\psi_1 - \Psi\left(R\left(0\right), R_d\left(0\right)\right)\right), \tag{71}$$

where ψ_1 is defined as

$$\psi_1 = \frac{1}{k_R}\left[\frac{1}{2} e_\Omega\left(0\right) \cdot J e_\Omega\left(0\right) + k_R \Psi(R\left(0\right), R_d\left(0\right))\right]. \tag{72}$$

Proof. Given the initial conditions (70) and (71), (68) can be written as

$$\begin{aligned} &k_R \Psi\left(R\left(t\right), R_d\left(t\right)\right) + \frac{1}{2}\tilde{\theta}_J^T \Gamma_J^{-1} \tilde{\theta}_J \leq V_2\left|_{C_2=0}\right.\left(t\right) \\ &\leq V_2\left|_{C_2=0}\right.\left(0\right) < k_R \psi_1 + \frac{1}{2}\tilde{\theta}_J^T \Gamma_J^{-1} \tilde{\theta}_J, \end{aligned}$$

which guarantees (69). □

In the translational dynamics, Lyapunov function V_1 containing the position and velocity errors is defined as

$$V_1 = \frac{1}{2} k_x e_x^T e_x + \frac{1}{2} m e_v^T e_v + C_1 m e_x \cdot e_v + \frac{1}{2}\tilde{\theta}_m^T \Gamma_m^{-1} \tilde{\theta}_m, \tag{73}$$

which can be lower and upper bounded by

$$\begin{aligned} z_1^T M_{11} z_1 + \frac{1}{2}\tilde{\theta}_m^T \Gamma_m^{-1} \tilde{\theta}_m &\leq V_1 \\ &\leq z_1^T M_{12} z_1 + \frac{1}{2}\tilde{\theta}_m^T \Gamma_m^{-1} \tilde{\theta}_m, \end{aligned}$$

where $z_1 = \begin{bmatrix} \|e_x\|, & \|e_v\| \end{bmatrix}^T$, and M_{11} and M_{12} are defined as

$$M_{11} = \frac{1}{2}\begin{bmatrix} k_x & -C_1 m \\ -C_1 m & m \end{bmatrix},$$
$$M_{12} = \frac{1}{2}\begin{bmatrix} k_x & C_1 m \\ C_1 m & m \end{bmatrix},$$

and C_1 is a positive constant described in the subsequent analysis. Taking the time derivative of V_1 and substituting the closed-loop dynamics defined in (46) yields

$$\begin{aligned} \dot{V}_1 =& k_x e_x \cdot \dot{e}_x + e_v \cdot m\dot{e}_v + C_1 m\dot{e}_x \cdot e_v + C_1 e_x \cdot m\dot{e}_v \\ &+ \tilde{\theta}_m^T \Gamma_m^{-1} \dot{\tilde{\theta}}_m \\ =& k_x e_x \cdot e_v + mC_1 \|e_v\|^2 + (e_v + C_1 e_x) \cdot m\dot{e}_v - \tilde{\theta}_m^T \Gamma_m^{-1} \dot{\hat{\theta}}_m \\ =& k_x e_x \cdot e_v + mC_1 \|e_v\|^2 - \tilde{\theta}_m^T \Gamma_m^{-1} \dot{\hat{\theta}}_m \\ &+ (e_v + C_1 e_x) \cdot \left(-k_x e_x - k_v e_v + Y_m \tilde{\theta}_m - X \right). \end{aligned} \tag{74}$$

Substituting the update law of $\hat{\theta}_m$ in Proposition 1 into (74) yields

$$\begin{aligned} \dot{V}_1 =& -k_x C_1 \|e_x\|^2 - (k_v - mC_1)\|e_v\|^2 - k_v C_1 e_x \cdot e_v \\ &+ (e_v + C_1 e_x)^T \left(Y_m \tilde{\theta}_m \right) - \tilde{\theta}_m^T Y_m^T (e_v + C_1 e_x) \\ &- (e_v + C_1 e_x) \cdot X - k_m^{cl} \tilde{\theta}_m^T \mathcal{G}_m \tilde{\theta}_m \\ =& -k_x C_1 \|e_x\|^2 - (k_v - mC_1)\|e_v\|^2 - k_v C_1 e_x \cdot e_v \\ &- (e_v + C_1 e_x) \cdot X - k_m^{cl} \tilde{\theta}_m^T \mathcal{G}_m \tilde{\theta}_m. \end{aligned} \tag{75}$$

The upper bound of X can be obtained from the force control input (18), (21), and the desired attitude (36), (37). Rewriting (18) as $f = \vec{f} \cdot Re_3 = \left(\left\| \vec{f} \right\| R_d e_3 \right) \cdot Re_3$ with (36), X becomes

upper bounded as follows:

$$\begin{aligned} X &= \frac{f}{e_3^T R_d^T R e_3} \left[\left(e_3^T R_d^T R e_3 \right) R e_3 - R_d e_3 \right] \\ &\leq \frac{\left\| \vec{f} \right\| e_3^T R_d^T R e_3}{e_3^T R_d^T R e_3} \left\| \left(e_3^T R_d^T R e_3 \right) R e_3 - R_d e_3 \right\|, \\ &\leq \left\| \vec{f} \right\| \left\| \left(e_3^T R_d^T R e_3 \right) R e_3 - R_d e_3 \right\| \end{aligned} \tag{76}$$

where the last term $\left\| \left(e_3^T R_d^T R e_3 \right) R e_3 - R_d e_3 \right\|$ represents the sine of the angle between Re_3 and $R_d e_3$, and $\|e_R\|$ represents the sine of the eigenaxis rotation angle between R_d and R:

$$\begin{aligned} \left\| \left(e_3^T R_d^T R e_3 \right) R e_3 - R_d e_3 \right\| &\leq \|e_R\| \\ &= \sqrt{\Psi \left(2 - \Psi \right)} \\ &\leq \alpha, \end{aligned} \tag{77}$$

where $\alpha \triangleq \sqrt{\psi_1 \left(2 - \psi_1 \right)} < 1$ based on Proposition 3. Therefore, based on (18) and (77), (76) can be upper bounded by

$$\|X\| \leq \left(k_x \|e_x\| + k_v \|e_v\| + B \right) \|e_R\| . \tag{78}$$

Substituting (78) into (75) yields

$$
\begin{aligned}
\dot{V}_1 \leq & -k_x C_1 \|e_x\|^2 - (k_v - mC_1) \|e_v\|^2 - k_v C_1 e_x \cdot e_v \\
& + (\|e_v\| + C_1 \|e_x\|) (k_x \|e_x\| + k_v \|e_v\| + B) \|e_R\| \\
& - k_m^{cl} \tilde{\theta}_m^T \mathcal{G}_m \tilde{\theta}_m \\
\leq & -k_x C_1 \|e_x\|^2 - (k_v - mC_1) \|e_v\|^2 - k_v C_1 e_x \cdot e_v \\
& + k_x \|e_R\| \|e_x\| \|e_v\| + k_v \|e_R\| \|e_v\|^2 + B \|e_R\| \|e_v\| \\
& + k_x C_1 \|e_R\| \|e_x\|^2 + k_v C_1 \|e_R\| \|e_x\| \|e_v\| \\
& + C_1 B \|e_R\| \|e_x\| - k_m^{cl} \tilde{\theta}_m^T \mathcal{G}_m \tilde{\theta}_m \\
\leq & -[k_x C_1 (1-\alpha)] \|e_x\|^2 - [k_v (1-\alpha) - C_1 m] \|e_v\|^2 \\
& + C_1 k_v (1+\alpha) \|e_x\| \|e_v\| \\
& + \|e_R\| \{k_x \|e_x\| \|e_v\| + B \|e_v\| + C_1 B \|e_x\|\} \\
& - k_m^{cl} \tilde{\theta}_m^T \mathcal{G}_m \tilde{\theta}_m.
\end{aligned} \tag{79}
$$

Proposition 4. *The following inequality is true:*

$$
\|e_v(t)\| \leq \max \left\{ \|e_v(0)\|, \frac{B}{k_v (1-\alpha)} \right\} \triangleq e_{v_{\max}}. \tag{80}
$$

Proof. Supposing that $C_1 = k_x = 0$, e_x can drop from (73), and based on it being known that $\|e_R\| \leq 1$, (73) and (79) can be rewritten as

$$
V_1 \mid_{C_1 = k_x = 0} = \frac{1}{2} m \|e_v\|^2 + \frac{1}{2} \tilde{\theta}_m^T \Gamma_m^{-1} \tilde{\theta}_m \tag{81}
$$

$$
\begin{aligned}
\dot{V}_1 \mid_{C_1 = k_x = 0} \leq & -k_v (1-\alpha) \|e_v\|^2 + B \|e_v\| \\
\leq & -\frac{k_v}{2} (1-\alpha) \|e_v\|^2 \\
& - \frac{k_v}{2} (1-\alpha) \|e_v\|^2 + B \|e_v\| \\
\leq & -\frac{k_v}{2} (1-\alpha) \|e_v\|^2 + \frac{B^2}{2k_v (1-\alpha)},
\end{aligned} \tag{82}
$$

where the negative term $-k_m^{cl} \tilde{\theta}_m^T \mathcal{G}_m \tilde{\theta}_m$ was dropped from (79), and (81) and (82) imply that $\|e_v\|$ is bounded as (80). □

Based on (4) and Proposition 4, (79) can be bounded as

$$\dot{V}_1 \leq -z_1^T W_1 z_1 + z_1^T W_{12} z_2 - k_m^{cl} \tilde{\theta}_m^T \mathcal{G}_m \tilde{\theta}_m, \tag{83}$$

where W_1, W_{12} are defined as follows:

$$W_1 = \begin{bmatrix} k_x C_1 (1-\alpha) & -\frac{1}{2} C_1 k_v (1+\alpha) \\ -\frac{1}{2} C_1 k_v (1+\alpha) & k_v (1-\alpha) - C_1 m \end{bmatrix}$$
$$W_{12} = \begin{bmatrix} k_x e_{v,\max} + C_1 B & 0 \\ B & 0 \end{bmatrix}.$$

To ensure that $W_1, M_{11},$ and M_{12} are positive definite, C_1 is selected to satisfy

$$C_1 < \min\Big\{ \sqrt{\frac{k_x}{m}}, \frac{k_v (1-\alpha)}{m}, \frac{4 k_x k_v (1-\alpha)^2}{k_v^2 (1+\alpha)^2 + 4 m k_x (1-\alpha)} \Big\}. \tag{84}$$

Remark 6. Although m in (84) is unknown, its upper and lower bound can be obtained from best guesses.

4.3 Stability Analysis of the Overall System

Theorem 2. *The ICL controller developed in (18) and (33) ensures that the system defined by (1)–(4) can achieve asymptotic tracking in the sense of (17) provided that C_1 and C_2 defined in (56) and (56) and the initial condition*

$$\Psi (R(0), R_d(0)) < 1 \tag{85}$$

are satisfied.

Proof. Let $V = V_1 + V_2$ be a Lyapunov function for the system containing rotational and trans-

lational dynamics:

$$\begin{aligned} V =& V_1 + V_2 \\ =& \frac{1}{2} k_x e_x^T e_x + \frac{1}{2} m e_v^T e_v + C_1 m e_x \cdot e_v \\ &+ \frac{1}{2} e_\Omega \cdot J e_\Omega + k_R \Psi\left(R, R_d\right) + J C_2 e_R \cdot e_\Omega \\ &+ \frac{1}{2} \tilde{\theta}_m^T \Gamma_m^{-1} \tilde{\theta}_m + \frac{1}{2} \tilde{\theta}_J^T \Gamma_J^{-1} \tilde{\theta}_J. \end{aligned} \tag{86}$$

It can be shown that (86) is bounded by two positive-definite functions:

$$\begin{aligned} & z_1^T M_{11} z_1 + z_2^T M_{21} z_2 + \frac{1}{2} \tilde{\theta}_m^T \Gamma_m^{-1} \tilde{\theta}_m + \frac{1}{2} \tilde{\theta}_J^T \Gamma_J^{-1} \tilde{\theta}_J \\ \leq V \leq & z_1^T M_{12} z_1 + z_2^T M_{22} z_2 + \frac{1}{2} \tilde{\theta}_m^T \Gamma_m^{-1} \tilde{\theta}_m \\ & + \frac{1}{2} \tilde{\theta}_J^T \Gamma_J^{-1} \tilde{\theta}_J. \end{aligned}$$

Taking the time derivative of (86) and using (66) and (83) yields

$$\begin{aligned} \dot{V} =& \dot{V}_1 + \dot{V}_2 \\ \leq & - z_1^T W_1 z_1 + z_1^T W_{12} z_2 - z_2^T W_2 z_2 \\ & - k_J^{cl} \tilde{\theta}_J^T \mathcal{G}_J \tilde{\theta}_J - k_m^{cl} \tilde{\theta}_m^T \mathcal{G}_m \tilde{\theta}_m, \end{aligned}$$

where matrices W_1, W_2 are positive definite and condition $\lambda_{\min}\left(W_2\right) > \frac{4\|W_{12}\|^2}{\lambda_{\min}(W_1)}$ guarantees that $\dot{V}$ is negative definite as long as the initial conditions (54) and (70) are satisfied, where W_2 is defined in (67), and therefore errors e_x, e_v, e_R, and e_Ω go to zero as time goes to infinity, as defined in (17). □

Remark 7. Theorem 2 requires that the initial attitude error is less than 90^0 (i.e., $\Psi\left(R\left(0\right), R_d\left(0\right)\right) < 1$) to achieve exponential stability. Suppose that this condition is not satisfied, i.e., $1 \leq \Psi\left(R\left(0\right), R_d\left(0\right)\right) < 2$, the attitude controller designed in (33) can be applied since it guarantees that the attitude error function Ψ decreases exponentially fast based on Theorem 1, and therefore, it enters the region of attraction of Theorem 2 (i.e., (85)) in finite time. Therefore, by combining Theorem 1 and Theorem 2, almost global exponential attractiveness can be achieved when $\Psi\left(R\left(0\right), R_d\left(0\right)\right) < 2$.

Chapter 5 Simulations

The simulations were conducted in a open-source simulator RotorS[29] in ROS Gazebo[30]. A six-rotor multirotor with an allocation matrix as defined in (7) was used as our model in ROS Gazebo with a simulation duration of 50 sec.

5.1 Setup and Ground Truth

The model, parameters, and control gains of the multirotor are presented in Fig. 3, Table 2, and Table 3, respectively. N_m and N_J as used for ICL are listed in Table 4. The ground truth of moment of inertia J and mass m in Table 2 were unknown parameters to be estimated in the simulations, and were used for evaluating the estimate error but not for implementing the controller.

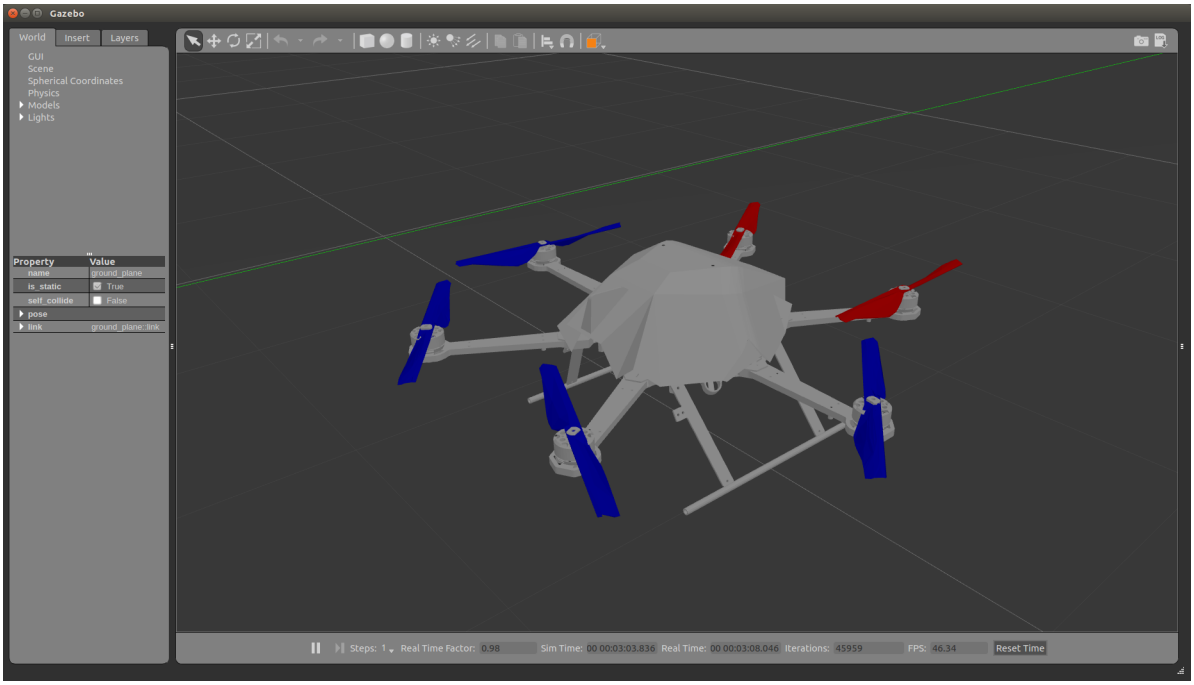

Figure 3: The multirotor model in Gazebo.

Table 2: Parameters used in the Gazebo simulations

Parameter	Value	Unit
m	1.568	kg
J	diag $[0.035, 0.046, 0.0977]$	kg $\cdot$ m^2
d	0.215	m

Table 3: Control gains used in the Gazebo simulations

Control Gain	Value
k_x	6
k_v	4.7
k_R	3
k_Ω	0.52
k_m^{cl}	0.002
k_J^{cl}	0.02
C_1	0.6
C_2	0.01

Table 4: N_m and N_J used in the ICL controller in the Gazebo simulations

Parameter	Value
N_m	20
N_J	45

The multirotor was initially stationary on the ground and was commanded to track a desired trajectory x_d and desired yaw direction $\vec{X}_{B_d}$ designed as

$$x_d = \begin{bmatrix} r \cdot \mathrm{c}\left(\frac{2 \cdot \pi t}{T}\right) + r \cdot \mathrm{c}\left(\frac{\pi t}{T}\right) + r \cdot \mathrm{c}\left(\frac{0.14 \cdot \pi t}{T}\right) \\ r \cdot \mathrm{s}\left(\frac{2.6 \cdot \pi t}{T}\right) + r \cdot \mathrm{s}(\frac{1.4 \cdot \pi t}{T}) + r \cdot \mathrm{s}(\frac{0.06 \cdot \pi t}{T}) \\ 1.3 \end{bmatrix},$$

$$\vec{X}_{B_d} = \begin{bmatrix} 0 \\ 1 \\ 0 \end{bmatrix},$$

where $r = 2$, $T = 280 \cdot \pi$, and c $(\cdot)$ and s $(\cdot)$ are abbreviations of cos $(\cdot)$ and sin $(\cdot)$, respectively. The desired altitude of the multirotor was 1.3 m, and $\vec{X}_{B_d}$ was chosen to be the unit vector in the direction of the y-axis in the inertial frame.

The initial states and estimates were

$$
\begin{aligned}
x(0) &= [-0.45, 6.2, 0]\,, \\
v(0) &= [0, 0, 0]\,, \\
R(0) &= \begin{bmatrix} 1 & 0 & 0 \\ 0 & 1 & 0 \\ 0 & 0 & 1 \end{bmatrix}, \\
\Omega(0) &= [0, 0, 0]\,, \\
\hat{\theta}_m(0) &= 0, \\
\hat{\theta}_J(0) &= [0, 0, 0]\,.
\end{aligned}
$$

5.2 Results

The tracking errors of the position, velocity, attitude, and angular velocity converged asymptotically to zero, as shown in Fig. 4 to Fig. 7. These findings verify that the multirotor with the developed ICL controller is able to track a desired trajectory without knowledge of the moment of inertia or mass. The $(\cdot)_1$, $(\cdot)_2$, and $(\cdot)_3$ notations in the following figures represent the first, second, and third elements of the corresponding vector, respectively.

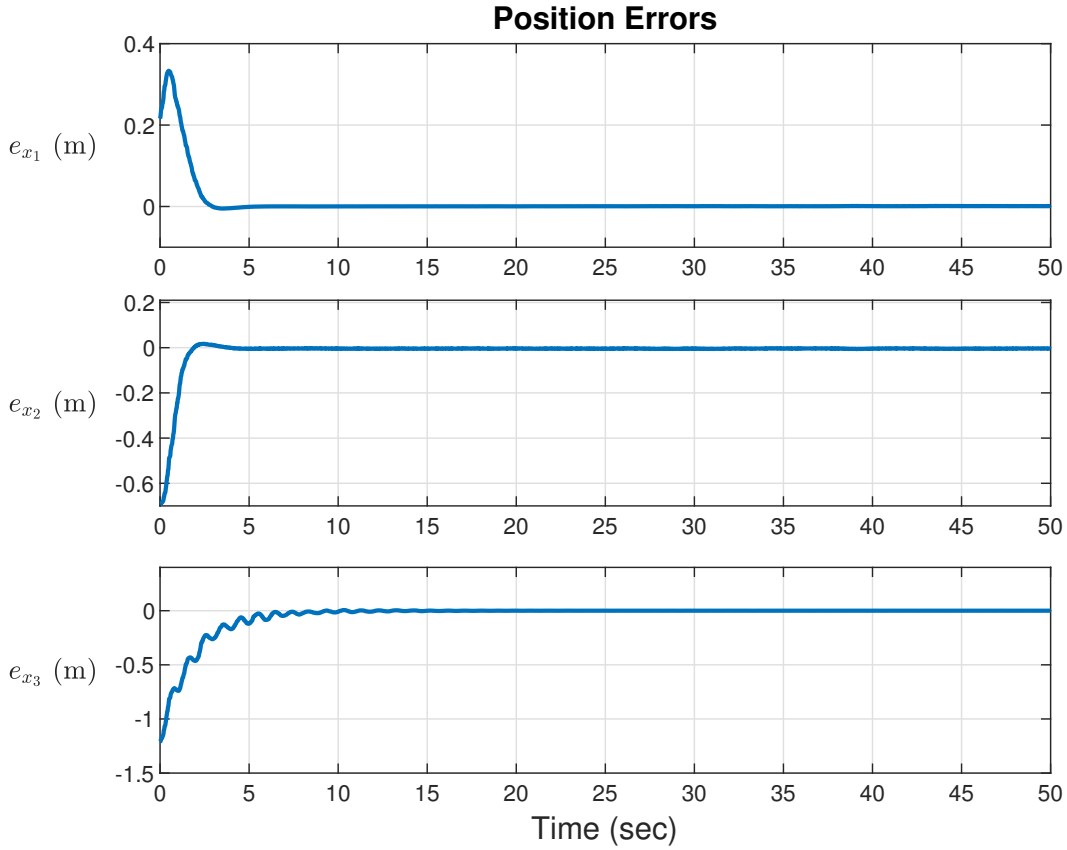

Figure 4: Position error trajectories.

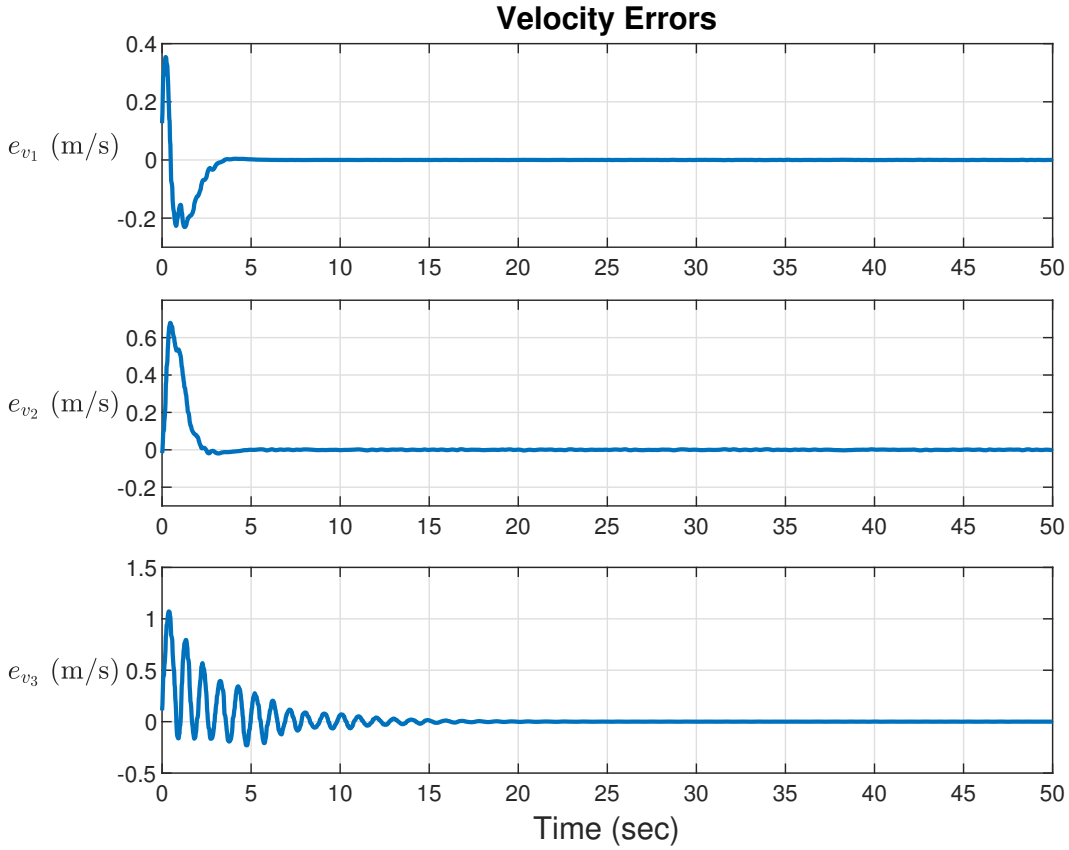

Figure 5: Velocity error trajectories.

The attitude error and the angular velocity error defined in (11) and (12) are shown in Fig. 6 and Fig. 7, respectively.

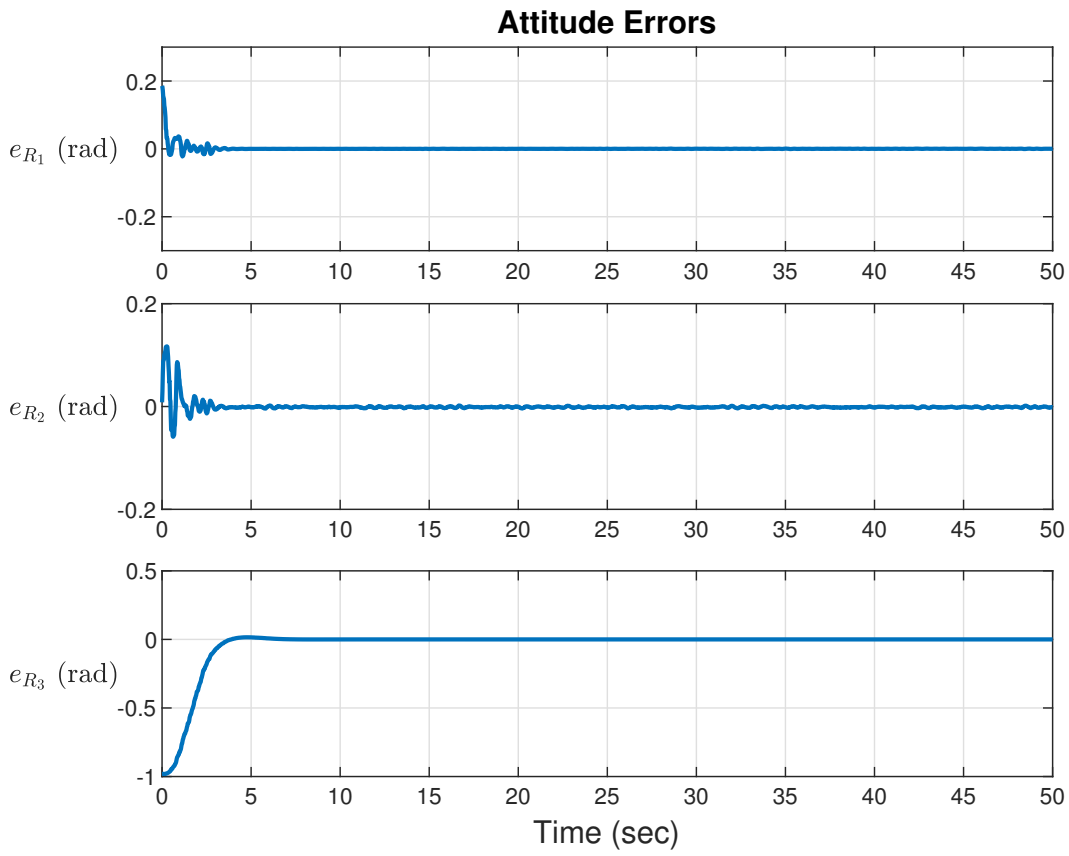

Figure 6: Attitude error trajectories.

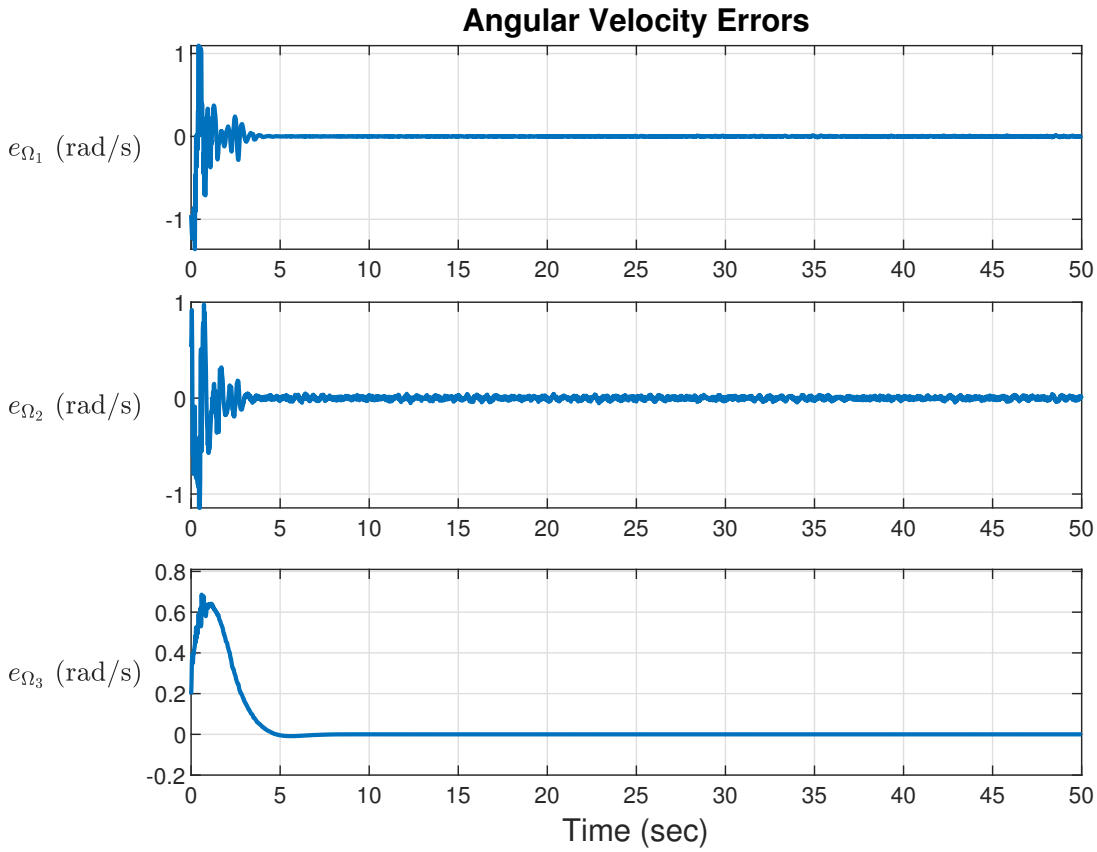

Figure 7: Angular velocity error trajectories.

Fig. 8 shows the estimates of the moment of inertia and mass during flight. The estimated values of the moment of inertia converged to diag $[0.033, 0.051, 0.091]$ after about 4 sec, which are close to the ground truth listed in Table 2. The estimated mass of the multirotor converged to 1.543 kg after about 15 sec, which is also close to the ground truth.

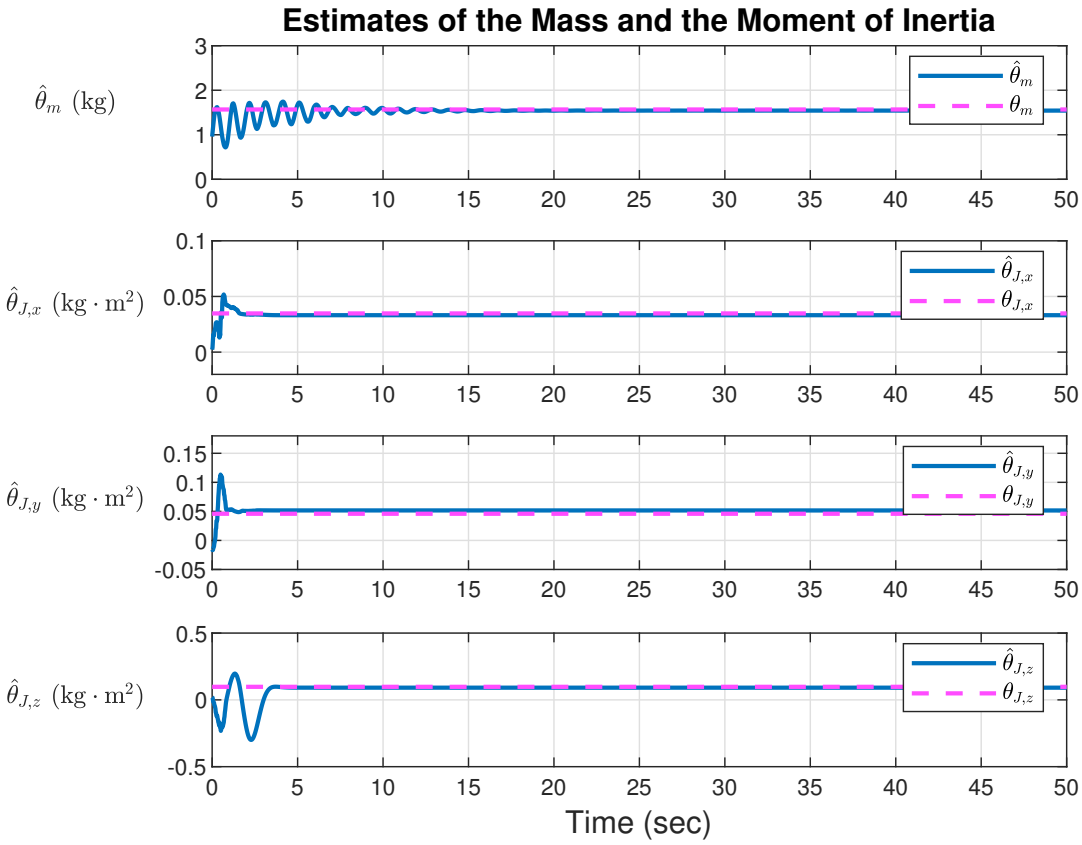

Figure 8: Estimates of the moment of inertia and mass.

The normalized estimate errors of the moment of inertia and mass were 7.9% and 1.5%, respectively, as shown in Fig. 9.

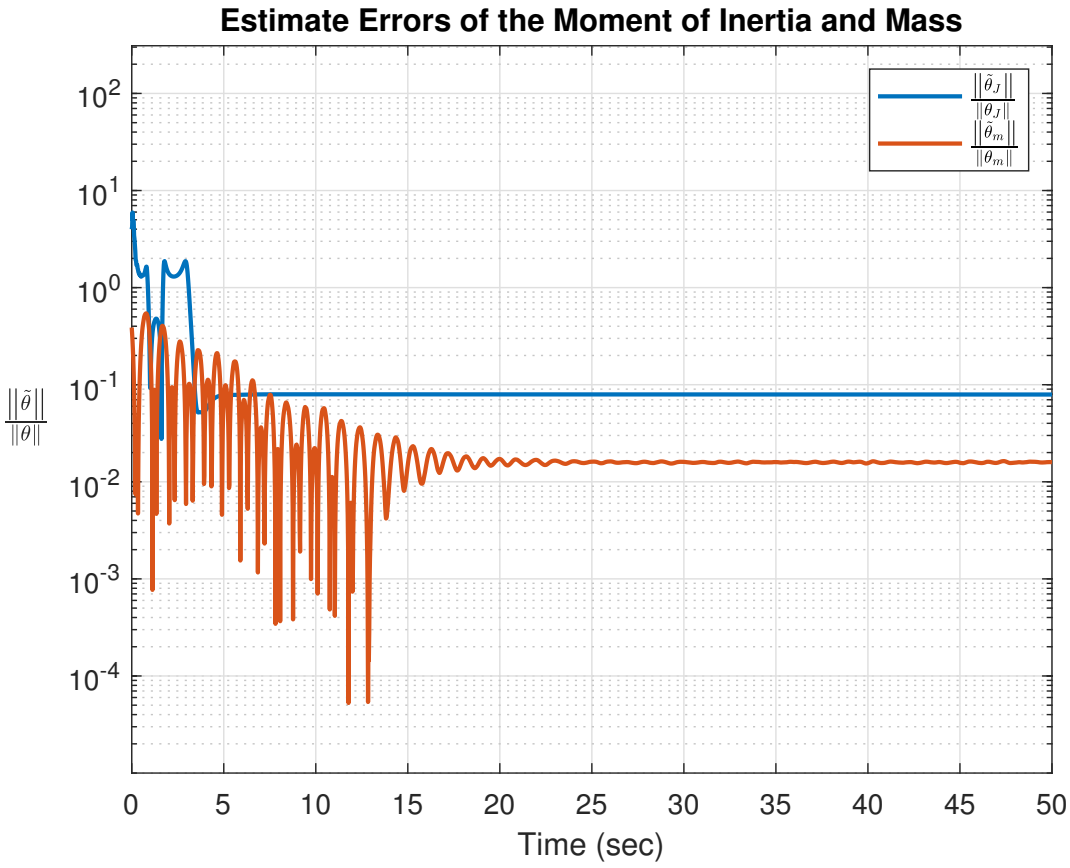

Figure 9: Normalized estimate errors of the moment of inertia and mass.

Fig. 10 compares the controller performance without and with the ICL controller, which demonstrates the importance and robustness of our developed controller. Since the mass of the multirotor significantly influences the system in Z direction, the position errors in that direction were compared between using the two kinds of controller. The estimate error of the mass was 0.132 kg when not using the ICL controller, whereas it was very close to zero when using the developed ICL controller. The figure also shows that there was a steady-state error when the ICL controller was not applied, which was eliminated when using the ICL controller.

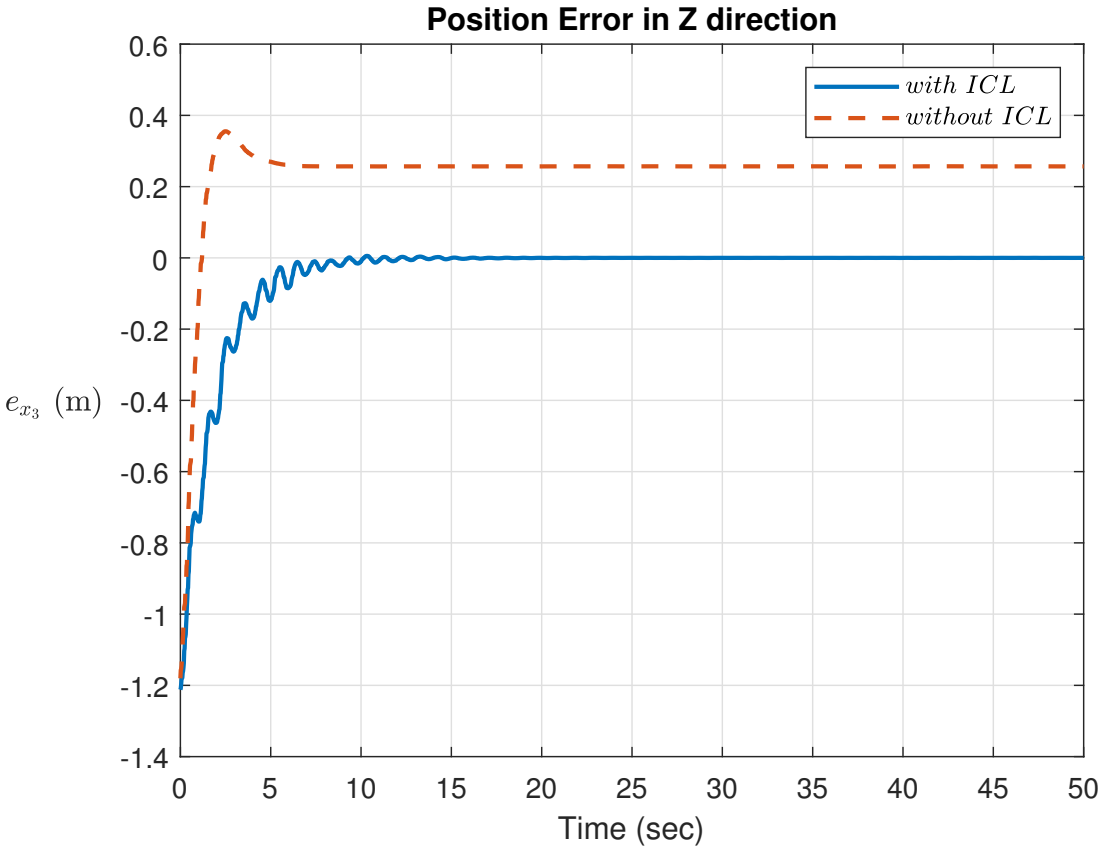

Figure 10: Controller performance in Z direction with and without the ICL controller. The case without the ICL controller is only controlled by the geometric tracking controller[11].

Fig. 11 compares the estimated parameters when using the adaptive controller and the developed ICL controller. Asymptotic convergence of The estimate errors converged asymptotically when using the ICL controller, whereas they converged to the wrong values when using the adaptive controller.

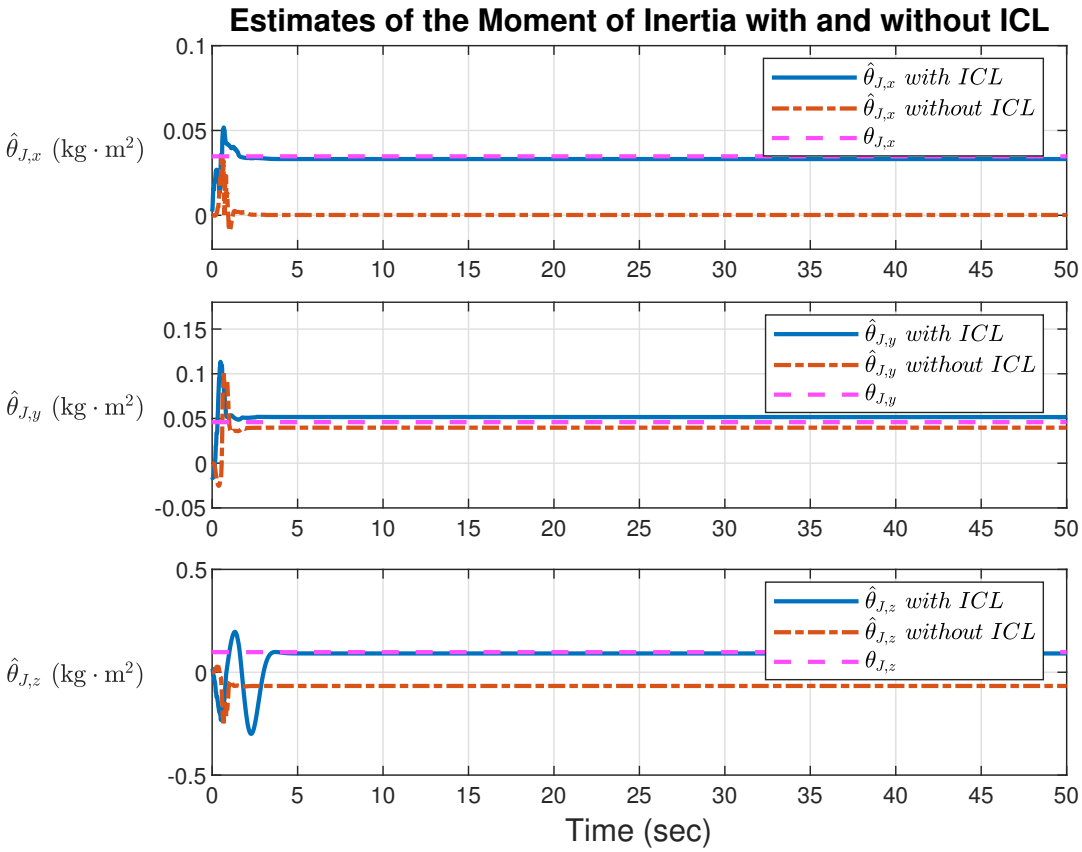

Figure 11: Comparison of the estimate errors using the adaptive controller and the ICL controller.

Chapter 6 Experiments

In this section, the experimental results using developed ICL controller are presented. We used a four-rotor multirotor with an allocation matrix defined as

$$\begin{bmatrix} f \\ M_1 \\ M_2 \\ M_3 \end{bmatrix} = \begin{bmatrix} 1 & 1 & 1 & 1 \\ -d & d & d & -d \\ d & d & -d & -d \\ -c_{\tau f} & c_{\tau f} & -c_{\tau f} & c_{\tau f} \end{bmatrix} \begin{bmatrix} f_1 \\ f_2 \\ f_3 \\ f_4 \end{bmatrix}$$

in the flight experiments. We show the accuracy of the parameter estimator and demonstrate the ability of the ICL controller to track a desired trajectory. Moreover, the comparison between geometric controller, adaptive controller, and the ICL controller is presented.

6.1 Hardware Architecture

A DJI F450 frame of multirotor is deployed as the hardware architecture to implement the ICL controller in the experiments. XBee modules are equipped to the multirotor to communicate between the multirotor and the ground station. Angular velocity and acceleration for obtaining the attitude of the multirotor are measured from inertial measurement unit (IMU), and the position of the multirotor is measured from motion capture system (Optitrack) with 12 cameras. The configuration of the multirotor is shown in Fig. 12.

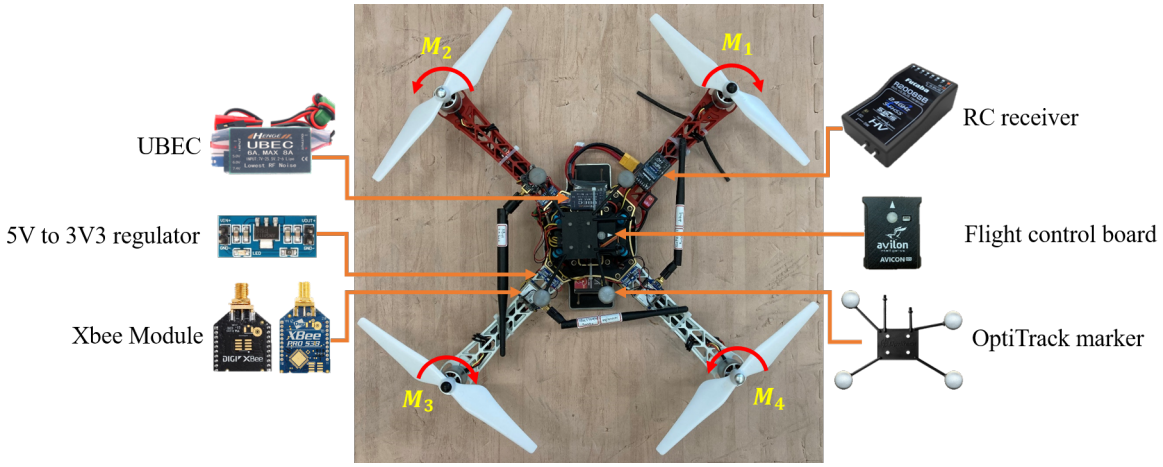

Figure 12: Hardware architecture.

The ground truth parameters, control gains, and parameters used in ICL controller are listed

in Table 5, Table 6, and Table 7, respectively. The ground truth of moment of inertia is obtained by establishing the mathematical model of the multirotor and the ground truth of mass is measured on the scales. The ground truth of moment of inertia J and mass m in Table 5 were unknown parameters to be estimated in the experiments, and were used for evaluating the estimate error but not for implementing the controller.

Table 5: Parameters used in the experiments

Parameter	Value	Unit
m	1.16	kg
J	diag $[0.013, 0.013, 0.024]$	$\text{kg} \cdot \text{m}^2$
d	0.225	m

Table 6: Control gains used in the experiments

Control Gain	Value
k_x	4
k_v	2
k_R	2.95
k_Ω	0.36
k_m^{cl}	2.5
k_J^{cl}	5
C_1	0.1
C_2	0.1

Table 7: N_m and N_J used in the ICL controller in the experiments

Parameter	Value
N_m	10
N_J	10

6.2 Trajectory Generation

To generate a smooth desired trajectory for the multirotor, [31] formulated the trajectory generation problem as a quadratic programming (QP) problem. We write the trajectory passing through given waypoints as piecewise polynomial function of order n as

$$s_i(t) = \sum_{j=0}^{n} \sigma_{ij} t^j, t_{i-1} \leq t < t_i, i \in \{1, 2, \cdots, m\},$$

where $n = 7$ is selected to obtain the minimum-snap trajectory, $m \in \mathbb{N}$ is the total numbers of segments of the trajectory, $\sigma_{ij} \in \mathbb{R}$ is the coefficient of j^{th} order of the polynomial. The quadratic problem for the minimum-snap trajectory is written with the cost function and the constraints involving initial condition, final condition, and the intermediate condition as

$$\min \int_{t_0}^{t_m} \left\| \frac{d^4 s_i}{d^4} \right\|^2 dt,$$

$$\text{s.t. } A\sigma = b.$$

6.3 Estimate Algorithm of the Angular Velocity

Since the ICL-based update law of the estimation of the moment of inertia in (40) involves angular velocity which is greatly affected by the sensor noise, an estimate algorithm of the angular velocity is designed. Rewritting the rotational dynamics of the multirotor (4) yields

$$\dot{\Omega} = \begin{bmatrix} \frac{M_1}{\hat{J}_{xx}} + \frac{\hat{J}_{yy}}{\hat{J}_{xx}}\Omega_2\Omega_3 - \frac{\hat{J}_{zz}}{\hat{J}_{xx}}\Omega_2\Omega_3 \\ \frac{M_2}{\hat{J}_{yy}} - \frac{\hat{J}_{xx}}{\hat{J}_{yy}}\Omega_1\Omega_3 + \frac{\hat{J}_{zz}}{\hat{J}_{yy}}\Omega_1\Omega_3 \\ \frac{M_3}{\hat{J}_{zz}} + \frac{\hat{J}_{xx}}{\hat{J}_{zz}}\Omega_1\Omega_2 - \frac{J_{yy}}{\hat{J}_{zz}}\Omega_1\Omega_2 \end{bmatrix}. \tag{87}$$

(87) can be used in the prediction part which is calculated in the computer as

$$\begin{aligned} \hat{\Omega}_k^- &= \hat{\Omega}_{k-1} + \dot{\Omega}_{k-1}\Delta t \\ &= \begin{bmatrix} \hat{\Omega}_{k-1,1} + \left(\frac{M_1}{\hat{J}_{xx}} + \frac{\hat{J}_{yy}}{\hat{J}_{xx}}\Omega_2\Omega_3 - \frac{\hat{J}_{zz}}{\hat{J}_{xx}}\Omega_2\Omega_3 \right) \cdot \triangle t \\ \hat{\Omega}_{k-1,2} + \left(\frac{M_2}{\hat{J}_{yy}} - \frac{\hat{J}_{xx}}{\hat{J}_{yy}}\Omega_1\Omega_3 + \frac{\hat{J}_{zz}}{\hat{J}_{yy}}\Omega_1\Omega_3 \right) \cdot \triangle t \\ \hat{\Omega}_{k-1,3} + \left(\frac{M_3}{\hat{J}_{zz}} + \frac{\hat{J}_{xx}}{\hat{J}_{zz}}\Omega_1\Omega_2 - \frac{\hat{J}_{yy}}{\hat{J}_{zz}}\Omega_1\Omega_2 \right) \cdot \triangle t \end{bmatrix}, \end{aligned}$$

where $\hat{J}_{xx}$, $\hat{J}_{yy}$, $\hat{J}_{zz}$ are the estimation of the moment of inertia and $\triangle t \in \mathbb{R}$ is the sampling time. The estimate of the angular velocity can be designed by combining the prediction part and the measurement part as

$$\hat{\Omega}_k = \hat{\Omega}_k^- + K_\Omega \left(\Omega - \hat{\Omega}_k^- \right),$$

where $K_\Omega \in \mathbb{R}^{3\times3}$ is the estimator gain and Ω is the angular velocity measurement from the gyroscope.

6.4 Estimate of the Mass

The estimate of the mass of the multirotor with ICL controller converged to 1.15 kg as shown in Fig. 13 with 1% error. This means the multirotor with the developed ICL controller is able to accurately estimate the mass during the flight.

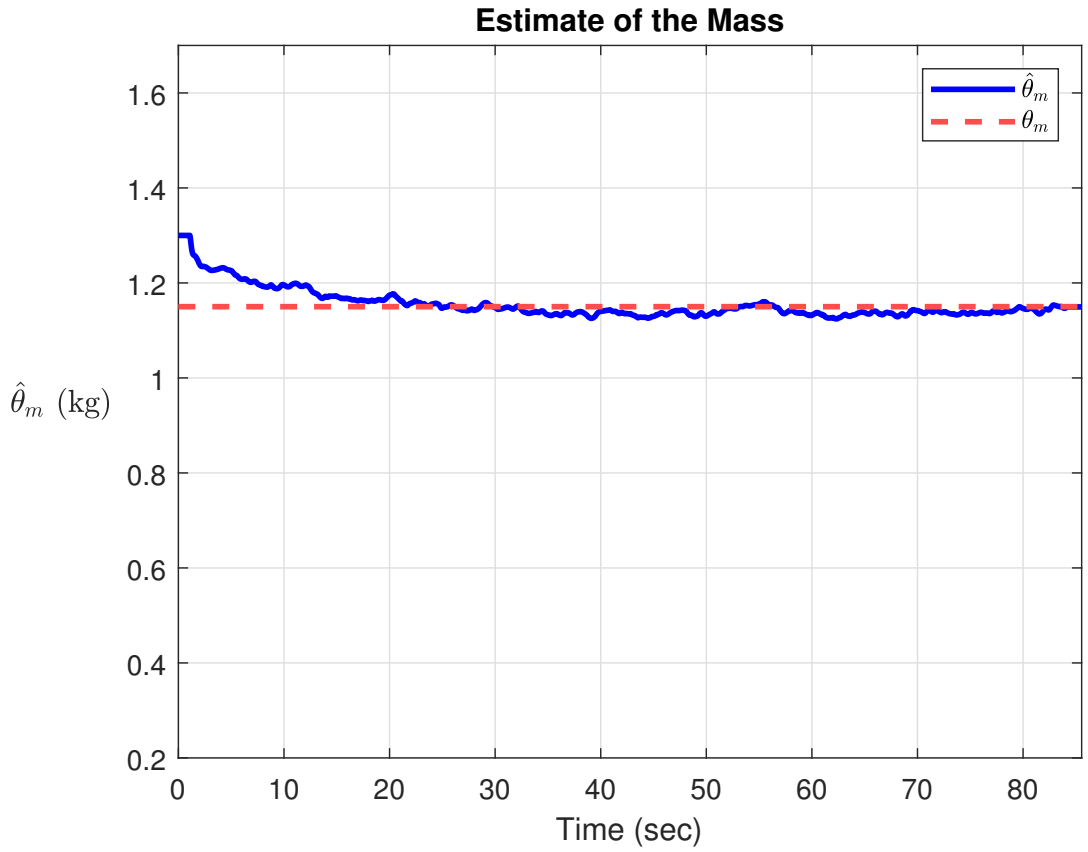

Figure 13: Estimate of the mass of the multirotor in the experiments. The red line represents the ground truth.

The accurate mass estimation makes the multirotor have better tracking performance in Z direction. The comparison of the tracking errors in Z direction with geometric controller (with constant mass from best guess) and ICL controller is presented in Fig. 14. It shows that there exists steady-state error in Z direction while using geometric controller. However, the steady-state error can be eliminated by using the developed ICL controller.

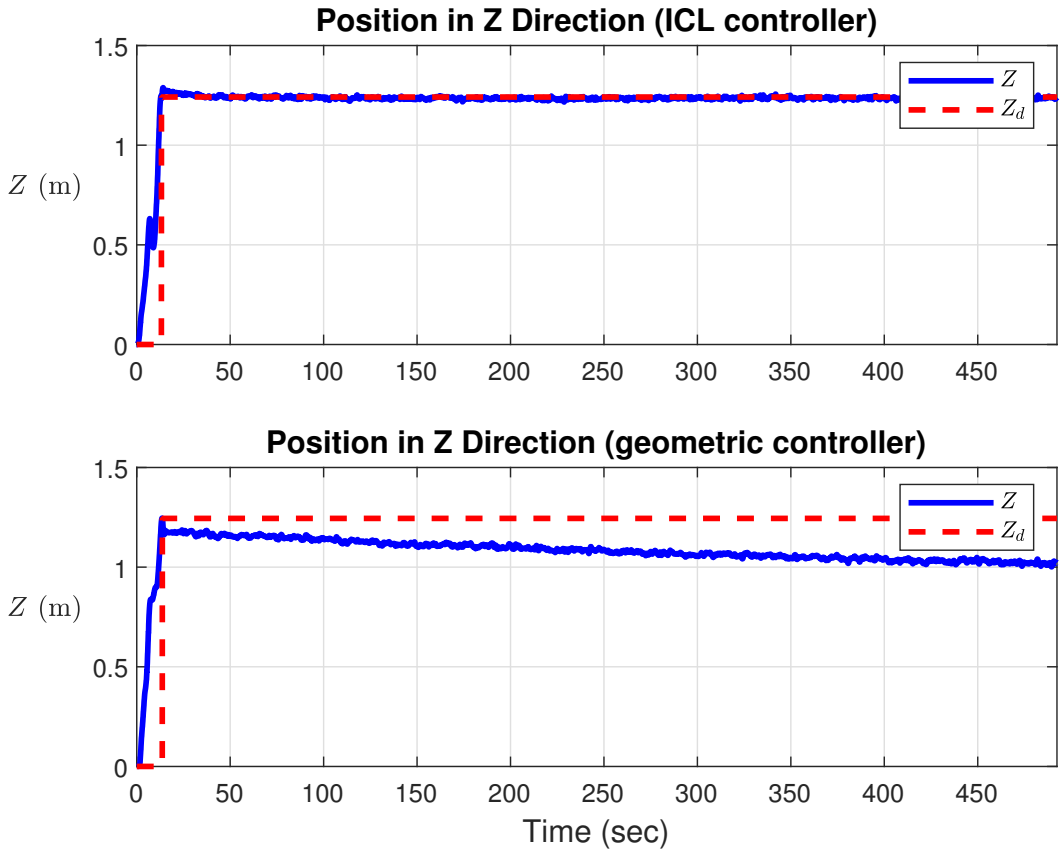

Figure 14: Comparison of position errors in Z direction.

6.5 Estimate of the Moment of Inertia

The estimate error of the moment of inertia using ICL controller is presented in Fig. 15. The moment of inertia estimation converge to $[0.013, 0.014, 0.022]$ $(\text{kg} \cdot \text{m}^2)$ with around 8% RMS error. The error can be attributed to the measurement noises since they can lead to inaccurate regression matrices through integration based on (39) and (41).

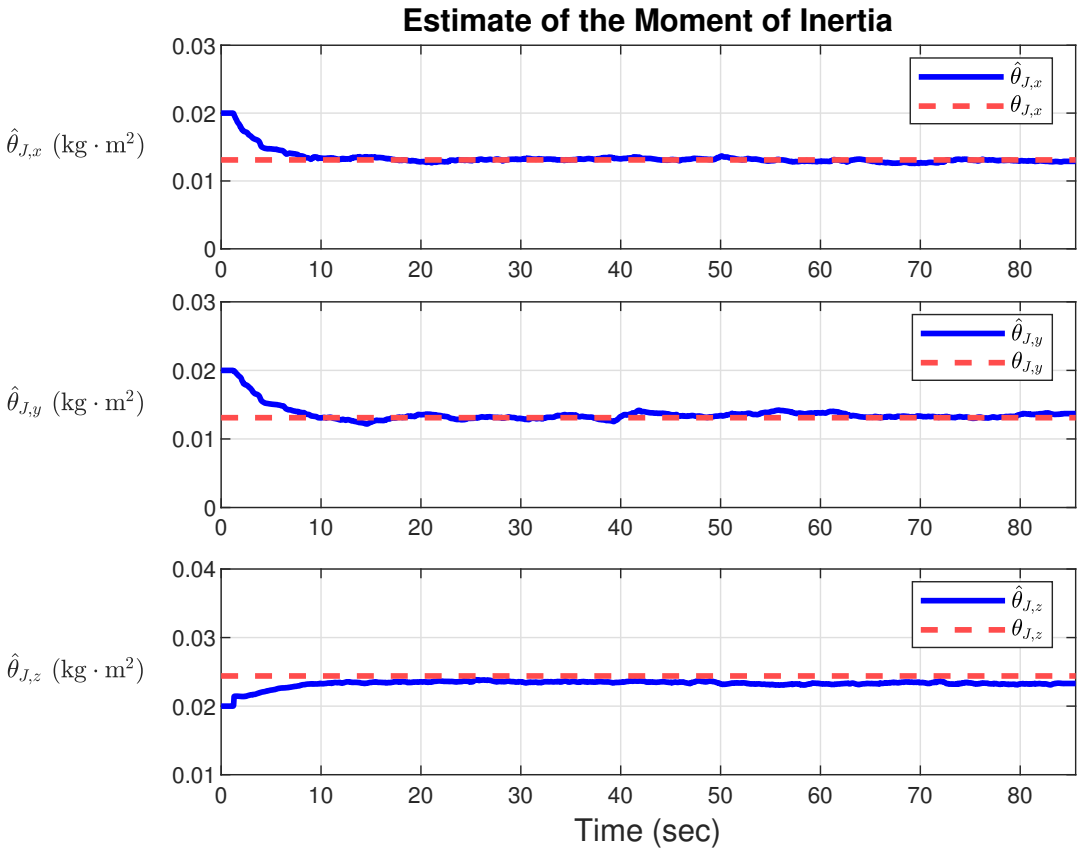

Figure 15: Estimate of the moment of inertia of the multirotor. Red lines represent the ground truth.

To further verify the efficacy of the developed ICL controller, multiple flights with different initial estimation values of the moment of inertia were conducted, and the estimate errors of the moment of inertia are presented in Fig. 16.

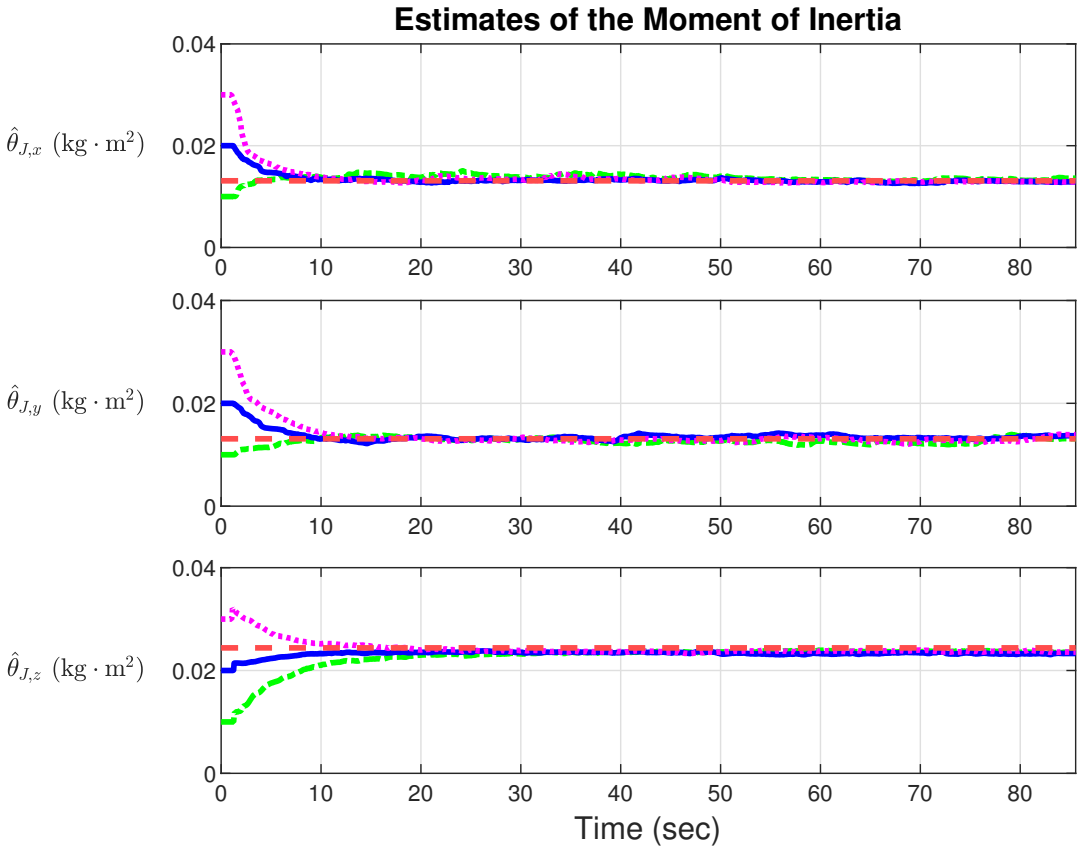

Figure 16: Estimate of the moment of inertia of the multirotor with different initial estimation value. The red line indicates the ground truth listed in Table 5. Other lines with different color indicate the moment of inertia estimation with different initial estimation value.

Fig. 17 compares the estimates of moment of inertia when using an adaptive controller and the developed ICL controller. The estimate errors converged asymptotically when using the ICL controller, whereas they converged to the wrong values when using the adaptive controller.

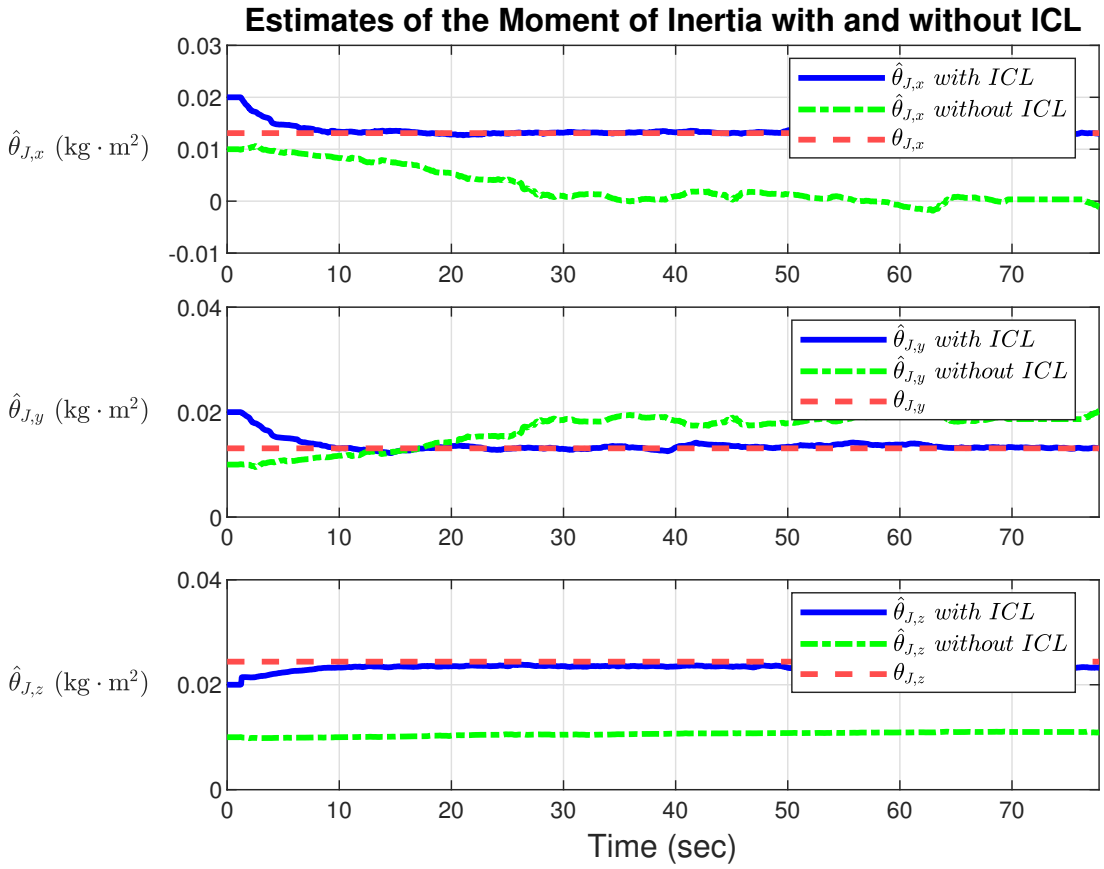

Figure 17: Comparison of the estimate errors using the adaptive controller and the ICL controller.

6.6 Tracking Performance

After a minimum-snap trajectory being generated in Section. 6.2, we test our ICL control algorithm on multiple runs of the trajectory. The trajectory tracking performance are presented in Fig. 18-20. These findings verify that the multirotor with the developed ICL controller is able to track a desired trajectory without knowledge of the mass and moment of inertia.

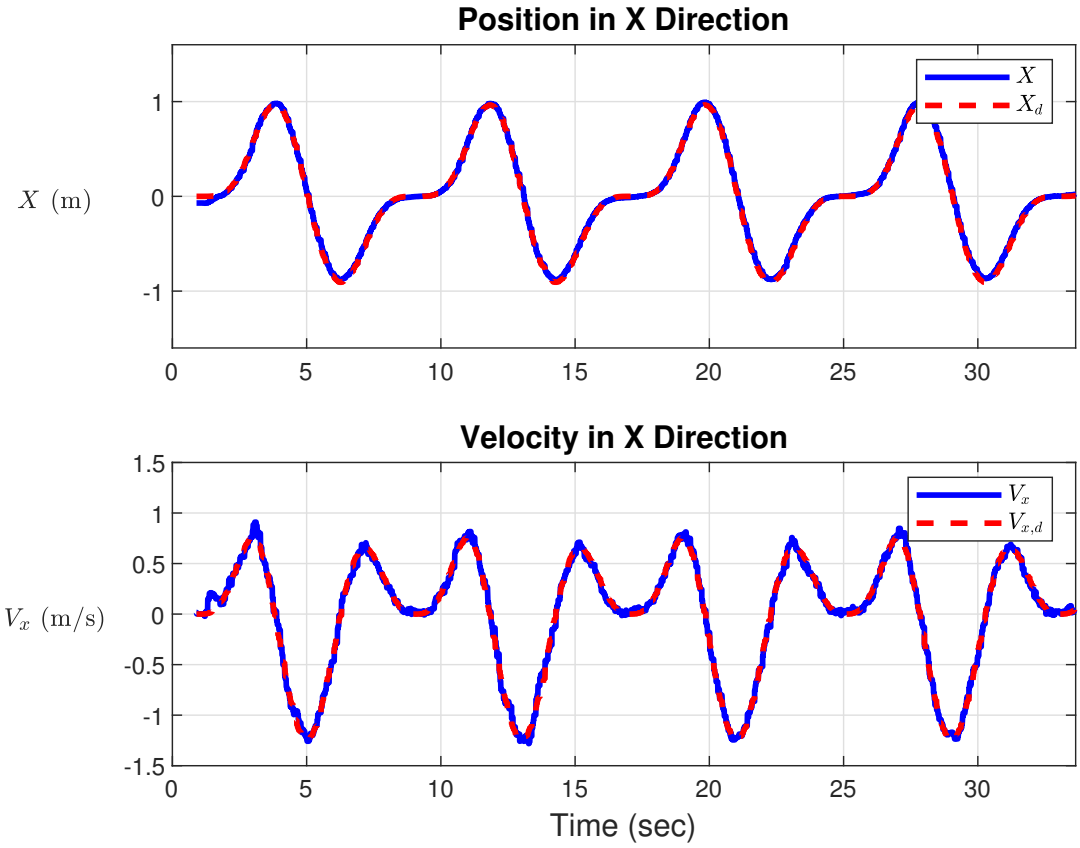

Figure 18: Tracking performance of the position and the velocity in X direction.

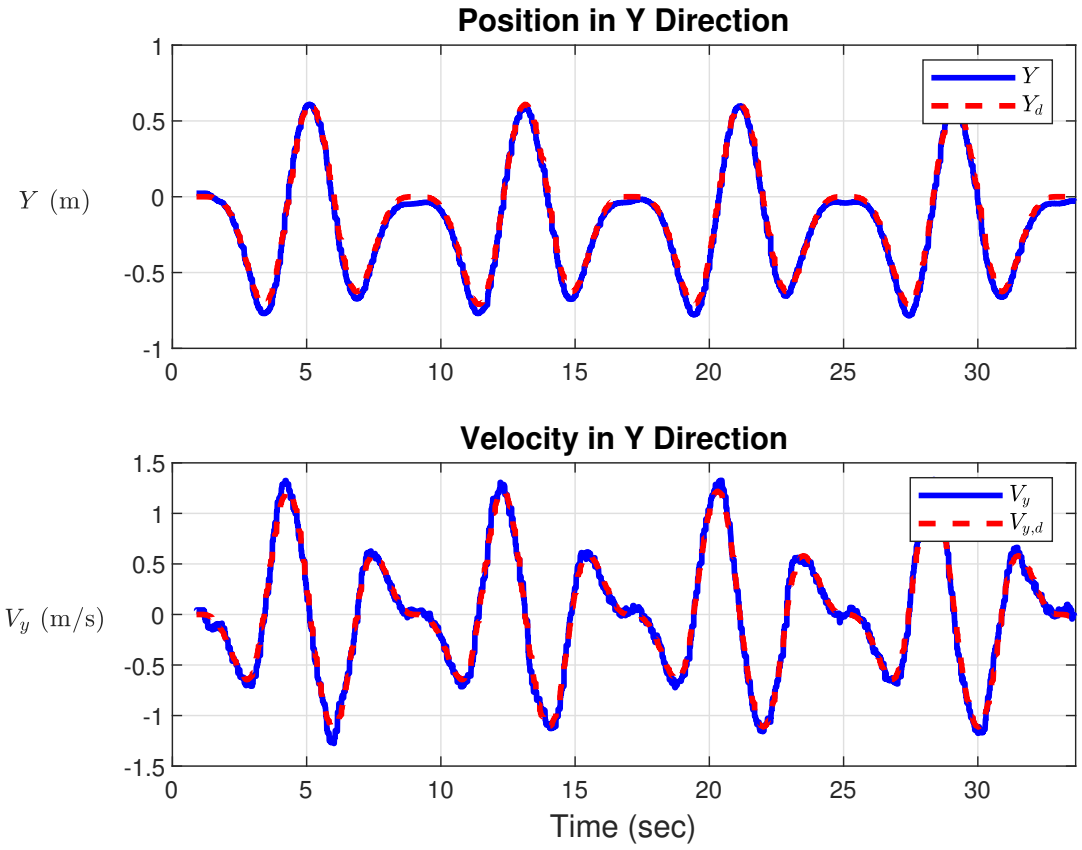

Figure 19: Tracking performance of the position and the velocity in Y direction.

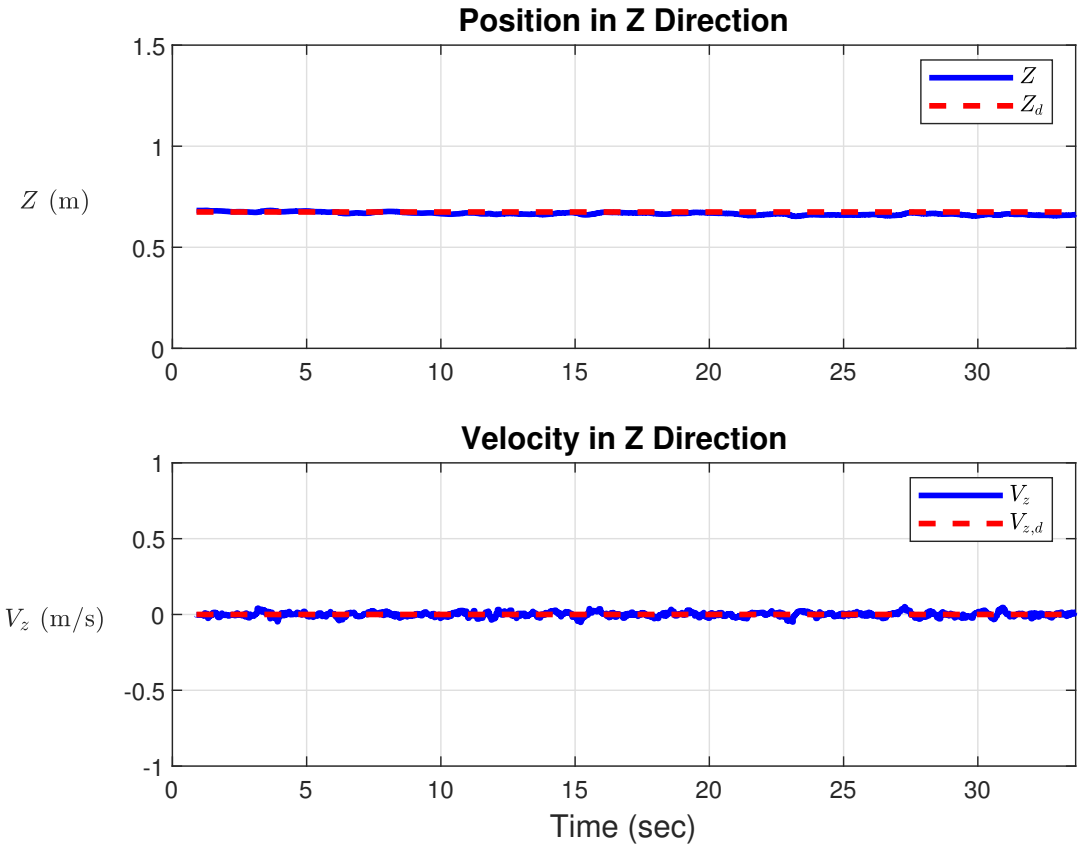

Figure 20: Tracking performance of the position and the velocity in Z direction.

The comparison of geometric controllers and ICL controllers in tracking performance are presented in Figs. 21-23, which show that the multirotor with ICL controller has better tracking performance since the estimate of the mass and the moment of inertia provide system knowledge to achieve good control performance. Moreover, the mass estimate with the ICL controller eliminates the steady-state error in Z direction as shown in Fig. 23.

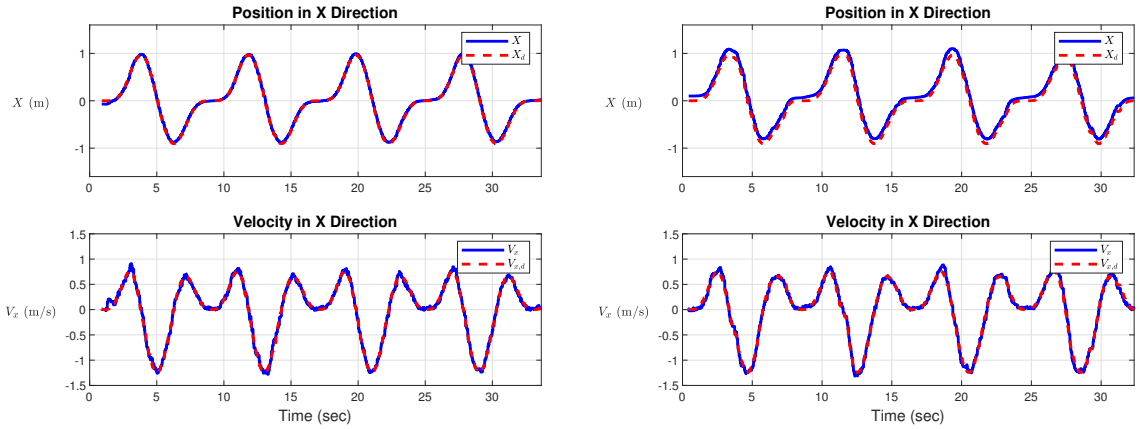

Figure 21: Tracking errors of the position and the velocity in X direction. Left) the tracking performance for the ICL controller, right) the tracking performance for the geometric controller.

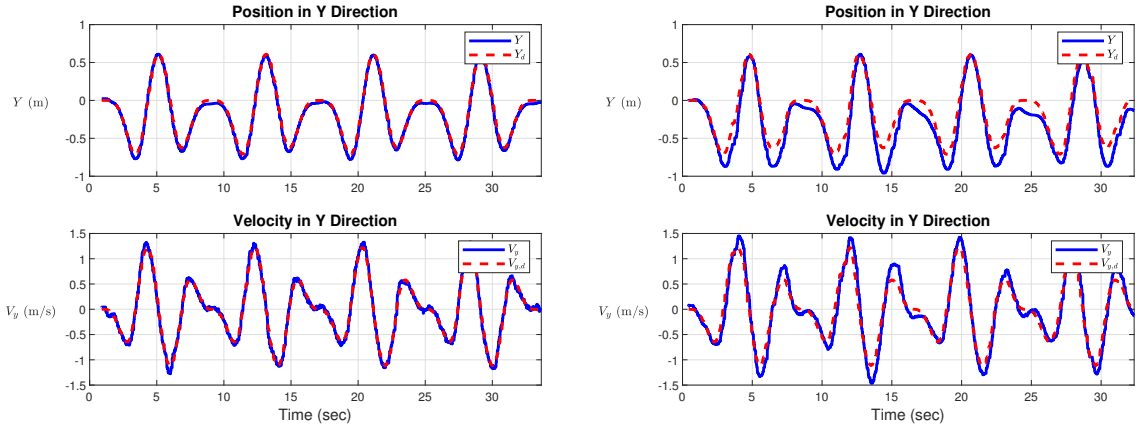

Figure 22: Tracking errors of the position and the velocity in Y direction. Left) the tracking performance for the ICL controller, right) the tracking performance for the geometric controller.

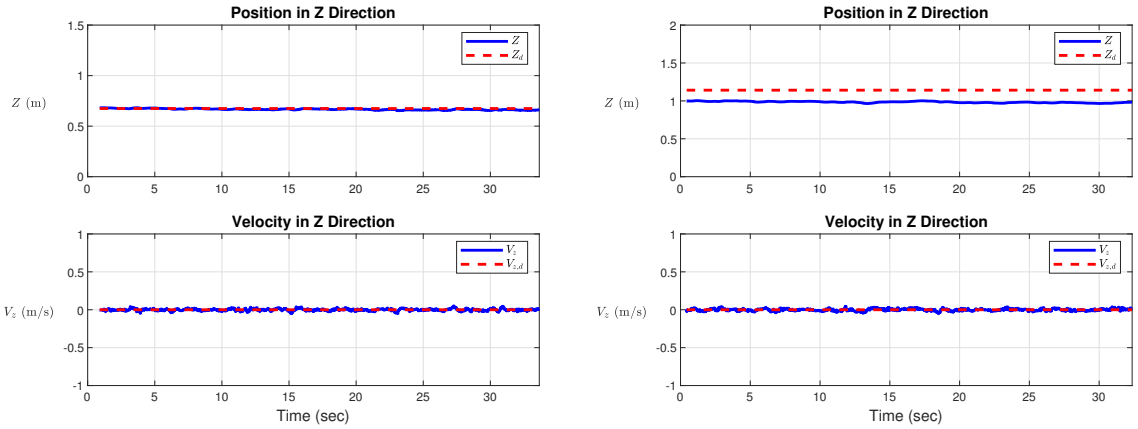

Figure 23: Tracking errors of the position and the velocity in Z direction. Left) the tracking performance for the ICL controller, right) the tracking performance for the geometric controller.

Chapter 7 Conclusion

An ICL controller has been developed for controlling a multirotor with unknown mass and moment of inertia. One of the main contributions of this work is that the developed ICL controller can be applied to many types of multirotors of unknown mass without the requirement of implementing extra sensors. The tracking errors and estimate errors of the unknown parameters were rigorously proven to exhibit asymptotic convergence. The stability of the ICL controller was verified in simulations and experiments. Compared to the geometric controller, the ICL controller ensures that steady-state errors in Z direction can be greatly reduced thanks to estimated mass. On the other hand, the ICL controller can outperform the adaptive controller since the adaptive controller cannot guarantee asymptotic convergence on the system parameters. Accurately estimating the system parameters using an ICL controller requires less human intervention before the flight and is thus crucial to achieving autonomous flight. The measurement noise is also an important factor in estimating the system parameters since it can cause the regression matrices to be less accurate.

Future work will include extending the current study to estimate other parameters of the multirotor, such as off-diagonal elements in the inertia matrix and the center of mass. Estimating the parameters online will avoid the need for an offline measurement procedure. Moreover, the stability of the multirotor system can still be ensured even when the geometric and inertia parameters are unknown.

References

[1] A. S. Aghdam, M. B. Menhaj, F. Barazandeh, and F. Abdollahi, "Cooperative load transport with movable load center of mass using multiple quadrotor UAVs," in *Int. Conf. Control Instrum. Autom.*, Qazvin Islamic Azad University, Qazvin, Iran, Jan. 2016, pp. 23–27.

[2] H. A. F. Almurib, P. T. Nathan, and T. N. Kumar, "Control and path planning of quadrotor aerial vehicles for search and rescue," in *SICE Annu. Conf. 2011*, Sep. 2011, pp. 700–705.

[3] M. A. Ma'sum, M. K. Arrofi, G. Jati, F. Arifin, M. N. Kurniawan, P. Mursanto, and W. Jatmiko, "Simulation of intelligent unmanned aerial vehicle (UAV) for military surveillance," in *2013 Int. Conf. on Adv. Comput. Sci. and Inf. Syst. (ICACSIS)*, Sep. 2013, pp. 161–166.

[4] J. Li and Y. Li, "Dynamic analysis and pid control for a quadrotor," in *2011 IEEE Int. Conf. on Mechatron. and Autom.*, 2011, pp. 573–578.

[5] A. L. Salih, M. Moghavvemi, H. A. F. Mohamed, and K. S. Gaeid, "Modelling and pid controller design for a quadrotor unmanned air vehicle," in *2010 IEEE Int. Conf. on Autom., Qual. and Test., Robot. (AQTR)*, vol. 1, 2010, pp. 1–5.

[6] S. Lee, S. H. Kang, and Y. Kim, "Trajectory tracking control of quadrotor UAV," in *2011 11th Int. Conf. on Control, Autom. and Syst.*, 2011, pp. 281–285.

[7] H. Voos, "Nonlinear control of a quadrotor micro-UAV using feedback-linearization," in *2009 IEEE Int. Conf. on Mechatron.*, 2009, pp. 1–6.

[8] D.-W. Lee, H. J. Kim, and S. Sastry, "Feedback linearization vs. adaptive sliding mode control for a quadrotor helicopter," *Int. J. of Control, Autom. and Syst.*, vol. 7, pp. 419–428, 2009.

[9] K. Runcharoon and V. Srichatrapimuk, "Sliding mode control of quadrotor," in *2013 The Int. Conf. on Technol. Adv. in Electr., Electron. and Comput. Eng. (TAEECE)*, 2013, pp. 552–557.

[10] E.-H. Zheng, J.-J. Xiong, and J.-L. Luo, "Second order sliding mode control for a quadrotor UAV," *ISA Trans.*, vol. 53, no. 4, pp. 1350 – 1356, 2014, disturbance Estimation and Mitigation.

[11] T. Lee, M. Leok, and N. H. McClamroch, "Geometric tracking control of a quadrotor UAV on SE(3)," in *IEEE Conf. on Decis. and Control*, 2010, pp. 5420–5425.

[12] D. Mellinger, Q. Lindsey, M. Shomin, and V. Kumar, "Design, modeling, estimation and control for aerial grasping and manipulation," in *2011 IEEE/RSJ Int. Conf. on Intell. Robot. and Syst.*, 2011, pp. 2668–2673.

[13] D. Ho, J. Linder, G. Hendeby, and M. Enqvist, "Mass estimation of a quadcopter using imu data," in *2017 Int. Conf. on Unmanned Aircr. Syst. (ICUAS)*, 2017, pp. 1260–1266.

[14] M. A. Al-Shabi, K. S. Hatamleh, and A. A. Asad, "UAV dynamics model parameters estimation techniques: A comparison study," in *2013 IEEE Jordan Conf. on Appl. Electr. Eng. and Comput. Technol. (AEECT)*, 2013, pp. 1–6.

[15] M. Y. Amir and V. Abbass, "Modeling of quadrotor helicopter dynamics," in *2008 Int. Conf. on Smart Manuf. Appl.*, April 2008, pp. 100–105.

[16] T. Bresciani, "Modelling, identification and control of a quadrotor helicopter," 2008, student Paper.

[17] W. Hussein, M. El-khatib, A. Elruby, and H. Haleem, "Quad rotor design simulation and implementation," in *Int. Conf. on Comput. Sci. from Algorithms to Appl.,(CSAA09)*, 2009.

[18] P. Pounds, R. Mahony, and P. Corke, "Modelling and control of a large quadrotor robot," *Control Eng. Pr.*, vol. 18, no. 7, pp. 691 – 699, 2010, special Issue on Aerial Robotics.

[19] J. Muliadi, R. Langit, and B. Kusumoputro, "Estimating the UAV moments of inertia directly from its flight data," in *2017 15th Int. Conf. on Qual. in Res. (QiR) : Int. Symp. on Electr. and Comput. Eng.*, July 2017, pp. 190–196.

[20] B. Mettler, M. Tischler, and T. Kanade, "System identification of small-size unmanned helicopter dyn." *Annu. Forum Proc. - Am. Helicopter Society*, vol. 2, pp. 1706–1717, Jan. 1999, proceedings of the 1999 55th Annual Forum of the American Helicopter Society, FORUM 55 ; Conference date: 25-05-1999 Through 27-05-1999.

[21] M. Burri, M. Bloesch, Z. Taylor, R. Siegwart, and J. Nieto, “A framework for maximum likelihood parameter identification applied on mavs,” *J. of Field Robot.*, vol. 35, no. 1, pp. 5–22, 2018.

[22] V. W□est, V. Kumar, and G. Loianno, “Online estimation of geometric and inertia parameters for multirotor aerial vehicles,” in *2019 Int. Conf. on Robot. and Autom. (ICRA)*, 2019, pp. 1884–1890.

[23] M. Imran Rashid and S. Akhtar, “Adaptive control of a quadrotor with unknown model parameters,” in *Proc. of 2012 9th Int. Bhurban Conf. on Appl. Sci. Technol. (IBCAST)*, 2012, pp. 8–14.

[24] C. Diao, B. Xian, Q. Yin, W. Zeng, H. Li, and Y. Yang, “A nonlinear adaptive control approach for quadrotor UAVs,” in *2011 8th Asian Control Conf. (ASCC)*, 2011, pp. 223–228.

[25] N. A. Chaturvedi, D. S. Bernstein, J. Ahmed, F. Bacconi, and N. H. McClamroch, “Globally convergent adaptive tracking of angular velocity and inertia identification for a 3-dof rigid body,” *IEEE Trans. on Control Syst. Technol.*, vol. 14, no. 5, pp. 841–853, 2006.

[26] A. Parikh, R. Kamalapurkar, and W. E. Dixon. (2015) Integral concurrent learning: Adaptive control with parameter convergence without PE or state derivatives. arXiv: 1512.03464.

[27] P. M. Patre, W. MacKunis, K. Kaiser, and W. E. Dixon, “Asymptotic tracking for uncertain dynamic systems via a multilayer neural network feedforward and RISE feedback control structure,” *IEEE Trans. Autom. Control*, vol. 53, no. 9, pp. 2180–2185, 2008.

[28] D. Shevitz and B. Paden, “Lyapunov stability theory of nonsmooth systems,” *IEEE Trans. Autom. Control*, vol. 39 no. 9, pp. 1910–1914, 1994.

[29] F. Furrer, M. Burri, M. Achtelik, and R. Siegwart, “Rotors - a modular gazebo mav simulator framework,” *Robot Operating System (ROS): The Complete Reference (Volume 1)*, pp. 595–625, 2016.

[30] N. Koenig and A. Howard, “Design and use paradigms for gazebo, an open-source multi-robot simulator,” in *Proc. IEEE/RSJ Int. Conf. Intell. Robot. Syst.*, vol. 3, Sept 2004, pp. 2149–2154 vol.3.

[31] D. Mellinger and V. Kumar, “Minimum snap trajectory generation and control for quadrotors,” in *Proc. IEEE Int. Conf. Robot. Autom.*, 2011, pp. 2520–2525.